

Lithological boundary detection using multi-sensor remote sensing imagery for geological interpretation

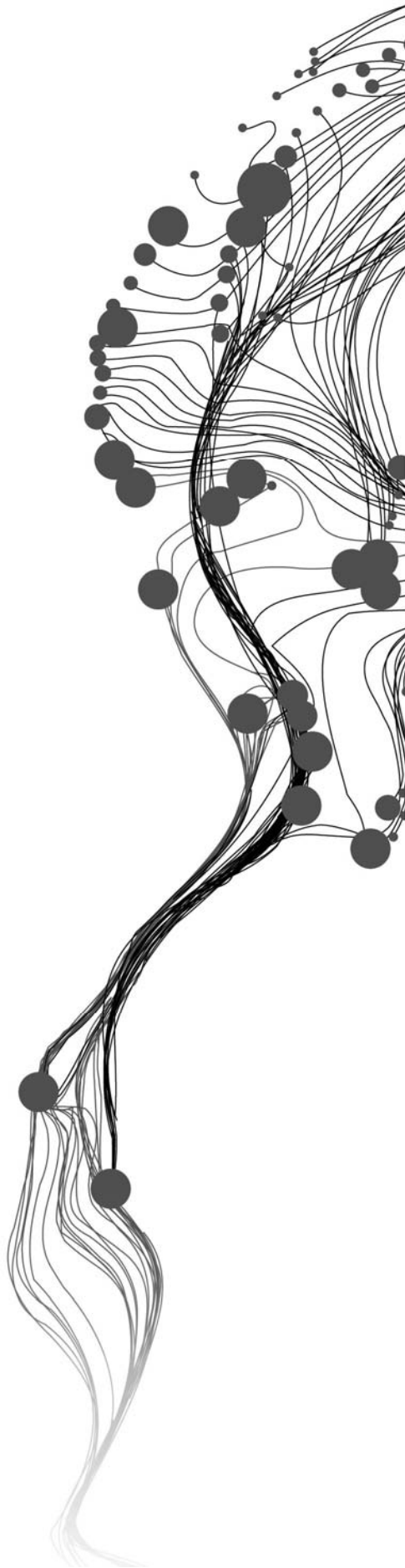
WOINSHET TAYE

March, 2011

SUPERVISORS:

Dr. F. J. A (Frank) van Ruitenbeek

Dr. H. M. A. (Harald) van der Werff



Lithological boundary detection using multi-sensor remote sensing imagery for geological interpretation

WOINSHET TAYE

Enschede, The Netherlands, March, 2011

Thesis submitted to the Faculty of Geo-Information Science and Earth Observation of the University of Twente in partial fulfilment of the requirements for the degree of Master of Science in Geo-information Science and Earth Observation.

Specialization: Applied Earth Sciences

SUPERVISORS:

Dr. F. J. A (Frank) van Ruitenbeek

Dr. H. M. A. (Harald) van der Werff

THESIS ASSESSMENT BOARD:

Prof. Dr. F.D. van der Meer (Chair)

Dr. D.G. Rossiter (External Examiner), Faculty of Geo-Information Science and Earth Observation of the University of Twente

Drs T.M. Loran (Observer)

Disclaimer

This document describes work undertaken as part of a programme of study at the Faculty of Geo-Information Science and Earth Observation of the University of Twente. All views and opinions expressed therein remain the sole responsibility of the author, and do not necessarily represent those of the Faculty.

ABSTRACT

Most processing methods for the interpretation of Lithological boundaries are done by classification of an image in to lithological units by spectral variation and then manually draw a boundary. In this way; identification of lithological boundaries cannot be consistent and is often influenced by the interpreter. The aim of this study is to determine whether edge detection algorithms detect and extract lithological boundaries. For this purpose edge detection and RTM template matching algorithms were used to extract lithological boundaries from remote sensing imagery.

Edge detection gradient in all direction using Euclidean measure used to measure spectral differences of neighbouring pixels. Edge detection was performed on thorium, uranium, thorium-uranium, thorium-uranium-potassium and analytical signal of total magnetic intensity. Edge maps are produced which show two spectrally contrasting regions in the image. The RTM template matching was applied to all images used in edge detection including the ASTER image. Region of interests were defined on different lithologies using field observation points and n the template for template matching. The algorithm give clear lines for the boundaries as defined in the template where ever contrasting signatures present in the image.

The results obtained from both methods were compared based on the position of boundary on geological map. From the comparison result the RTM method using thorium show better match pixels with the position of boundary to the geological map. From the multiple layers used thorium-potassium show the least performance of match pixel.

Threshold was applied to edge maps from RTM output ratio map in order to determine edge pixels. A buffer zone was made for the boundaries considered and the percent of pixels belong in the buffer zone was calculated at each thresholds. Ratio of pixels inside the buffer zone to pixels outside are constant for most of the ratio images at each threshold points which indicate that increasing the threshold have effects on both outside and inside pixels.

The results obtained show that RTM performs well in detecting lithological boundaries as defined in the template; edge detection shows relatively good performance.

ACKNOWLEDGEMENTS

I would like to express my sincere gratitude to the Netherlands Government through the Netherlands fellowship program (NFP) for granting me the opportunity to follow the study. I am very grateful to my employer, Geological Survey of Ethiopia for supporting me to fulfil my wish.

I am greatly indebted to my first supervisor Dr. van Frank Ruitenbeek for his guidance and encouragement throughout my study period. I appreciate his critical comments and scientific suggestions during the research work. My gratitude also goes to my second supervisor Dr. H. M. A. van der werff for his valuable comments and guidance.

My very special thank goes to Drs. Tom Loran course director AES for his unreserved support and help during my problem and allowing me come back and finish my study.

I greatly acknowledge all my instructors for giving me knowledge during the study period.

I am grateful to Dr. Tsai Woldai for his support and care during the field work. I also would like to extend my gratitude to my colleagues who were together with me during the field work for their help and warm sprits. I also wish to express my appreciation to all my classmates for their friendship, support and socialization.

Dr Nigel Stack from FUGRO Airborne services and Dr. Sally Barritt from Geowitch are greatly acknowledged for their assistance to get the high resolution airborne data and the department of geological survey and mines (DGSM) of Uganda permit us to use the data.

My profound gratitude goes to my whole family for their valuable support, mentally and spiritually being there for me.

TABLE OF CONTENTS

1.	INTRODUCTION.....	1
1.1.	General.....	1
1.2.	Problem statement.....	1
1.3.	Research objectives.....	2
1.4.	Research questions.....	2
1.5.	Out line of chapters.....	2
2.	LITERATURE REVIEW.....	3
2.1.	Edges and edge detection algorithms.....	3
2.1.1.	Edge filter (hyperspectral edge detection).....	3
2.1.2.	Template matching.....	4
2.2.	Works done.....	5
2.3.	Gamma ray data.....	5
2.4.	Magnetic data.....	7
2.5.	ASTER.....	7
3.	STUDY AREA.....	9
3.1.	Location.....	9
3.1.1.	Regional geology.....	10
3.1.2.	Local geology.....	10
4.	MATERIALS AND METHODS.....	11
4.1.	Materials.....	11
4.2.	Software.....	11
4.3.	Methods.....	11
4.3.1.	Preparation for field work.....	12
4.3.2.	Field observations.....	12
4.3.3.	Image pre processing.....	13
4.3.4.	Methods to apply edge detection algorithms.....	14
5.	RESULTS AND DISCUSSION.....	15
5.1.	Lithological boundaries determined in the field.....	15
5.2.	Processed images.....	17
5.3.	Edge detection.....	20
5.3.1.	Applied to gamma ray spectrometry.....	20
5.3.2.	Applied to Analytical signal of total magnetic intensity.....	22
5.4.	RTM template matching.....	23
5.4.1.	Applied to gamma ray spectrometry.....	23
5.4.2.	Applied to analytical signal of total magnetic intensity.....	26
5.4.3.	Applied to ASTER ratio image.....	26
5.5.	Comparison of edge detection results.....	27
5.5.1.	Edge detection RTM template matching results.....	27
5.5.2.	Influence of threshold.....	29
6.	CONCLUSION AND RECOMMENDATION.....	37

LIST OF FIGURES

Figure 2-1: Schematic drawing of a template a) A template consists of a value range and margin (m) on both sides of template and centre pixel (cp), b) it is moved over the image and c) rotates at every pixel position at user defined increments (van Ruitenbeek et al., 2008).....4

Figure 2-2: Variation in average K, Th & U content in igneous rocks with increasing Si content (B.L. Dickson & Scott, 1997)6

Figure 3-1: Location of study area, source from (R.J. Johnson and Williams, 1961) 9

Figure 4-1: General workflow of the methods used.....12

Figure 4-2: Field observation location points13

Figure 4-3: Quartzite unite, picture taken looking to the east from gneiss side.....13

Figure 4-4: Showing areas where roi's defined for template design on thorium images. Red circles are areas where roi's defined for the template design for boundary between gneiss and quartzite and (a) for sandstone and granite (b). The red plus signs are observation points14

Figure 5-1: Selected cross section lines produced across boundaries at some field observation points15

Figure 5-2: Profiles across boundary between granitic gneiss and quartzite. It shows the location of estimated boundary zone from field observations in relation to elevation and rock units.16

Figure 5-3 : Profiles across boundary between sandstone and granite. It shows the location of estimated boundary from field observations in relation to elevation and rock units17

Figure 5-4: Processed images subset to focus on boundary between granitic gneiss and quartzite18

Figure 5-5: Processed images subset to focus on boundary between sandstone and granite.....19

Figure 5-6: Edge maps produced from a) thorium, b) uranium, c) potassium, d) thorium-uranium, e) potassium-thorium and f) potassium-thorium-uranium images. The red line indicates the position of boundary between granitic gneiss and quartzite on geological map21

Figure 5-7: Edge images produced from a) thorium, b) uranium, c) potassium, d) thorium-uranium, e) potassium-thorium and f) potassium-thorium-uranium images. The red line indicates the position of boundary between sandstone and granite on geological map22

Figure 5-8: Edge maps produced from analytical signal of total magnetic intensity image23

Figure 5-9: Template matching results of a)thorium, b) uranium, c) potassium, d) thorium-uranium, e) potassium-thorium and f)potassium-thorium-uranium for boundary between gneiss and quartzite. the white line indicates the position of boundary on geological map24

Figure 5-10: Template matching results of a)thorium, b) uranium, c) potassium, d) thorium-uranium, e) potassium-thorium and f)potassium-thorium-uranium for boundary between sandstone and granite. The white line indicates the position of boundary on geological map25

Figure 5-11: Template matching result from Analytical signal. The white line indicates the position of boundary on geological map.....27

Figure 5-12: Template matching result from ASTER ratio images. The white line indicates the position of boundary on geological map.....27

Figure 5-13: maps showing buffers of 200m around boundary one (a) and two (b) on geological map overlain on ratio maps28

Figure 5-14: Comparison of template matching (a) and edge detection (b) results using 200m buffer area on both b1 and b2 on geological map.29

Figure 5-15: 80m buffer area around the boundaries detected.....29

Figure 5-16:Ratio image of throiim showing b1 at initial threshold (a), graph showing distribution of detected pixels on the entire area. the DN value are converted to logarithmic scale in order to empasize the significance of values at the tail of the histogram and considered as edge pixels (b) and the third graph

shows the percentage of pixels detected inside and outside the buffer zone and also their ratio as the threshold increases (c)..... 31

Figure 5-17: Ratio image of uranium showing boundary one at initial threshold (a), graph showing distribution of detected pixels on the entire area. the DN value are converted to logarithmic scale in order to empasize the significance of values at the tail of the histogram and considered as edge pixels (b) and the third graph shows the percentage of pixels detected inside and outside the buffer zone and also their ratio as the threshold increases (c) 31

Figure 5-18: Ratio image of throim-uranium showing boundary one at initial threshold (a), graph showing distribution of detected pixels on the entire area. the DN value are converted to logarithmic scale in order to empasize the significance of values at the tail of the histogram and considered as edge pixels (b) and the third graph shows the percentage of pixels detected inside and outside the buffer zone and also their ratio as the threshold increases (c) 32

Figure 5-19 : Ratio image of throim-uranium-potassium showing boundary one at initial threshold (a), graph showing distribution of detected pixels on the entire area. the DN value are converted to logarithmic scale in order to empasize the significance of values at the tail of the histogram and considered as edge pixels (b) and the third graph shows the percentage of pixels detected inside and outside the buffer zone and also their ratio as the threshold increases (c) 33

Figure 5-20: Ratio image of thorium showing boundary two at initial threshold (a), graph showing distribution of detected pixels on the entire area. the DN value are converted to logarithmic scale in order to empasize the significance of values at the tail of the histogram and considered as edge pixels (b) and the third graph shows the percentage of pixels detected inside and outside the buffer zone and also their ratio as the threshold increases (c) 34

Figure 5-21: Ratio image of uranium showing boundary two at initial threshold (a), graph showing distribution of detected pixels on the entire area. the DN value are converted to logarithmic scale in order to empasize the significance of values at the tail of the histogram and considered as edge pixels (b) and the third graph shows the percentage of pixels detected inside and outside the buffer zone and also their ratio as the threshold increases (c) 35

Figure 5-22: Ratio image of thorium-uranium showing boundary two at initial threshold (a), graph showing distribution of detected pixels on the entire area. the DN value are converted to logarithmic scale in order to empasize the significance of values at the tail of the histogram and considered as edge pixels (b) and the third graph shows the percentage of pixels detected inside and outside the buffer zone and also their ratio as the threshold increases (c)..... 35

Figure 5-23: Ratio image of thorium-uranium-potassium showing boundary two at initial threshold (a), graph showing distribution of detected pixels on the entire area. the DN value are converted to logarithmic scale in order to empasize the significance of values at the tail of the histogram and considered as edge pixels (b) and the third graph shows the percentage of pixels detected inside and outside the buffer zone and also their ratio as the threshold increases (c) 36

LIST OF TABLES

Table 4-1: Survey Specifications of FUGRO data acquisition..... 11

1. INTRODUCTION

1.1. General

Geological maps provide geological baseline information in mineral exploration to demarcate mineralized and non-mineralized areas. Geological mapping with remote sensing and geophysical data is widely employed due to cost effectiveness and capability of providing information of areas that are not easily accessible. Interpretation of remote sensing and geophysical imagery to delineate lithological units of economic interest involves the identification and mapping of lithological contacts and other geological boundaries. A lithological boundary is the contact surface between geological units with different mineralogical assemblage, for example contact of intrusive body, a stratigraphic contact or fault lines separating different units (Qureshi, 2005).

Multi-sensor remote sensing data provide different geological information on the surface cover and mapping of boundaries between geological units. Gamma ray spectroscopy data; for example, provides relative geochemical variations of radioelement concentrations in the upper 30-40cm of the earth's crust. This information can be used to map bed rock lithology, mineral alteration, and regolith materials in highly weathered and vegetated terrains. Optical remote sensing images on the other hand can be used for lithological mapping in areas with few vegetation; and weathering cover (B.L. Dickson and Scott, 1997; Finn and Morgan, 2002).

In most processing techniques; determination of lithological boundaries is done by classification of an image in to lithological units by spectral variation and then manually draw a boundary. Identification of lithological boundaries cannot be consistent and is often influenced by the interpreter (van Ruitenbeek et al., 2008). Several image processing techniques have been developed for identification of lithological boundaries in a consistent and efficient way.

Edge detection algorithms are image processing technique that, automatically extract boundaries by applying local independent operators over an image (A.L. Jaques 1997; Qureshi, 2005). Edge detectors help to reduce the data to be processed by retaining the most important properties of object boundary. Edge detection algorithms have been widely used on grey level images, but have also been extended to multi-band and hyperspectral images (Bakker and Schmidt, 2002).

Hyperspectral and template matching algorithms are used in this research for detection of lithological boundaries in the study area. Rotation variant template matching algorithm (RTM) developed by (van der Werff et al., 2006) was used for detection of boundaries between gneiss- quartzite and sandstone-granite. The templates are designed to be one dimensional consisting of 5x1 pixel.

1.2. Problem statement

Geological image interpretation aims at identifying and mapping of lithological units and structural features. The interpretation and mapping of lithological boundaries using common pixel-based classification techniques is inefficient and depends on an interpreter's opinion (van Ruitenbeek et al., 2008). It is also a time consuming process and can be rather difficult if multiple data sets have to be analysed simultaneously (Mavrantza and Argialas, 2008). Edge detection algorithms are however consistent and automatically extract those boundary zones. The problem with edge detection is that, it extracts any kind of edges whether it belongs to geologic feature or not.

1.3. Research objectives

The objective of this research is to determine whether edge detection algorithms can be used to detect and extract lithological contacts and boundaries from multi-sensor remote sensing data that are relevant for geological mapping, and to investigate the type of lithological boundaries or contacts that can be detected by edge detection algorithms using different input data layers.

In order to fulfil the main objective the following specific objectives are defined:

- To characterize and map selected lithological contacts in the field.
- To test the capability of edge detection algorithms, such as template matching and hyperspectral edge detection, in the identification of the selected lithological contacts using aeromagnetic, gamma ray, ASTER and SRTM data sets.
- To investigate whether the use of multiple data layers increase the accuracy of boundary detection using edge detection algorithms
- To investigate the type of lithological boundaries or contacts (intrusive contacts, contacts that are covered by vegetation or weathering products, transitional or crisp) that can be detected by edge detection algorithms using different input data layers
- To investigate whether detected boundaries represent the actual geologic contacts that can be polygonized for geologic mapping or they reflect surface / sub surface features unrelated to lithological variations.

1.4. Research questions

- Do the selected lithological boundaries match with field observation contacts?
- How efficient are edge detection algorithms in delineating lithological contacts using aeromagnetic, gamma ray, ASTER and SRTM data sets?
- What is the contribution of using multiple data layer in increasing the accuracy of detecting lithological boundaries?
- Which type of lithological contacts/ boundaries can be detected by edge detection algorithms using different input data layers? (Lithological boundaries can be intrusive contacts, contacts that are covered by vegetation or weathering, gradational and crisp)
- Do the detected boundaries represent actual geologic contacts that can be used for geological mapping?

1.5. Out line of chapters

- Chapter one describes the general introduction of the thesis, problems, objectives and research questions
- Chapter two describes the literature reviews about the general working principles of edge detection algorithms; especially hyperspectral and template matching and the images used in the thesis
- Chapter three deals with the study area; location and geology
- Chapter four present the materials used and methods followed in the research work
- Chapter five describes the results obtained from field work, hyperspectral edge detection and RTM template matching along with discussions.
- Chapter six gives conclusions from the results obtained and recommendations

2. LITERATURE REVIEW

2.1. Edges and edge detection algorithms

In grey scale images, edges are characterized by the intensity change due to physical properties of an object such as geometry, illumination and reflectance, (Hou and Wei, 2002; Qureshi, 2005; Torre and Poggio, 1986 and Zhu et al., 1999). In multiband images more detailed information can be obtained to characterize an edge than in grey level images where intensity, hue and saturation play a combined role in determining whether edges or object boundaries are present in the image (Cheng, et al., 2001; Zhu et al., 1999).

Most image processing applications aim at the identification and extraction of edge/ boundaries in the image. Edge operators autonomously demarcate those portions of the image representing edges in the scene by first edge enhancing the input and subsequently utilizing a thresholding scheme to binarize the output (Qureshi, 2005). Edge images are usually used as input for higher image processing and analysis such as image segmentation and object recognition (Bakker and Schmidt, 2002); since edge operators reduce the amount of data to be processed by retaining the information of object boundary (Canny, 1986; Zhu et al., 1999). Edge operators have been widely used in grey level images in past, are improved to work on multispectral and hyperspectral images recently for the detection of object boundaries and lithological contacts (Bakker and Schmidt, 2002; Cumani, 1991).

A variety of edge detection algorithms have been developed in the history of computer vision systems and image processing. These algorithms differ in their purpose and their mathematical and algorithmic properties (Peli and Malah, 1982). Edge detection algorithms are generally grouped in to two categories based on the integration of edge detectors in to a computer vision system, the first categories include detectors which do not use a prior knowledge about the scene and edge to be detected while the second categories are contextual and are guided by the prior knowledge about the edge to be detected (Ziou and Tabbone, 1998). In case of this research edge detection and template matching are used.

2.1.1. Edge detection (hyperspectral edge detection)

Edge filters determine edges by measuring local spectral variability between neighbouring pixels. The simplest edge filters measure the difference or gradient between neighbouring pixels in 3x3 kernels. Difference or gradient of neighbouring pixels are averaged and high values are assigned to edge pixels while low values indicate local homogeneity (Bakker and Schmidt, 2002). The gradient differences in neighbouring pixels are calculated in different directions and produces different edge images. The edge images produced are gradient derived in X, Y, X and Y, up diagonal, down diagonal, up and down diagonal, combined XY and diagonal, differences of 4 neighbouring and differences of 8 neighbouring pixels. The measure of difference can be expressed in vector space and uses Euclidian distance, spectral angle, intensity difference, spectral information divergence and Bray Curtis difference. The most widely used distance measures well described by (Bakker and Schmidt, 2002) are Euclidean distance, spectral angle and intensity difference. Euclidean distance is influenced by intensity value unlike spectral angle measure which depends only on the angle between two pixels in feature space regardless of the length of the vectors. Euclidean distance represents the distance between two pixels in feature space such that high intensity value indicates high Euclidean distance and hence spectral dissimilarity. Lower angle in spectral angle measure indicates similarity (spectral match) between two pixels in feature space (Bakker and Schmidt, 2002).

2.1.2. Template matching

Template matching has been widely used in grey scale images for the detection of object boundaries, defect detection and face detection (Tsai and Yang, 2005). Rotation variant template matching (RTM) algorithm as contrast to other template matching algorithms, is designed to be rotationally variant. The rotation variance of the template contains information about the presence of boundary between spectrally contrasting surfaces in the image. The algorithm matches the spectral and spatial information of the object by moving and rotating user defined template on the image (van der Werff et al., 2006) A template is a miniature image designed to be odd dimensional such a way that, the centre pixel contains the information of the boundary between two spectrally contrasting surfaces. The value of the centre pixel is ignored in calculating the template fit in order to indicate the presence of crisp boundary (van Ruitenbeek et al., 2008) (Fig 2.1).

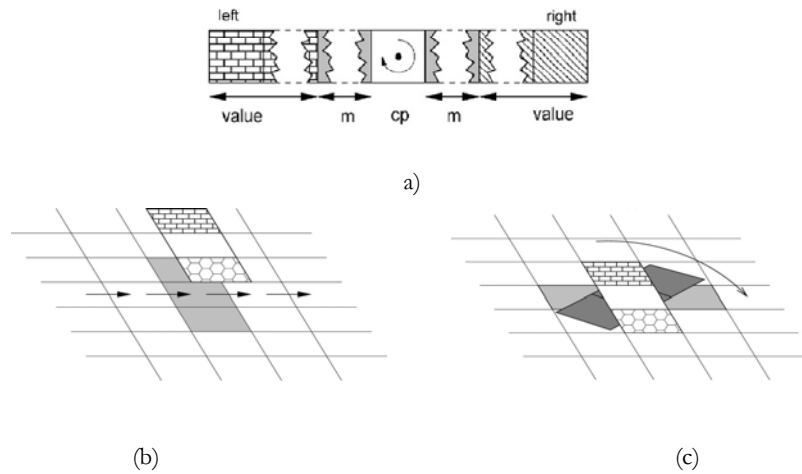


Figure 2-1: Schematic drawing of a template a) A template consists of a value range and margin (m) on both sides of template and centre pixel (cp), b) it is moved over the image and c) rotates at every pixel position at user defined increments (van Ruitenbeek et al., 2008).

When the template is moved and rotated on the image, statistical fit of the template is calculated at every position and orientation. The spatial fit of the template is expressed by mean and variance in spectral fit while the spectral fit of the template by Euclidian distance, intensity difference and spectral angle (van der Werff et al., 2006).

The output of the algorithm consists of measurements derived from template match. Six main measurements are derived from the algorithm which include, optimal fit, optimal template orientation, marginal fit, mean fit, rotation variance and mean spectral variance. Ratios of some of the measurements are also produced along with the main outputs. The following

The spectral fit is the measure of overall fit between each template pixel and the image pixel at every position and orientation “a”, so that it can be measured by distance measures in feature space, like spectral angle and Euclidian distance and others. Spectral fit is calculated as:

$$F_{s(a)} = \frac{\sum_{p=0}^N F(p)}{N}, \tag{2.1}$$

Where, $F(p)$ is the spectral fit for a pixel p and N is the number of template pixels.

The spectral variance measures the similarity /dissimilarity between template pixels and image pixels. High spectral variance V_s indicates that template pixels do not spectrally fit with image pixels and the variance in spectral fit of all template pixels at every orientation, V_s is calculated as

$$V_{s(a)} = \frac{\sum_{p=0}^N (F(p) - F_{s(a)})^2}{N}, \tag{2.2}$$

Optimal fit is best spectral fit between the template pixels and image pixel that is obtained when the template is rotated at every position, it can be measured by spectral angle (optimal angle Λ (opt)), or any distance measure in the feature space. Low Euclidian distance or low spectral angle between image pixels and template pixels indicate more similarity: hence optimal fit and vice versa.

The mean spectral fit at all orientation of the template fit is calculated as:

$$F_r = \frac{\sum_{a=0}^A F_s(a)}{A}, \quad (2.3)$$

The marginal fit is the maximum difference in template fit. The rotation variance (V_r) indicates the presence or absence of crisp boundary between spectrally contrasting surfaces. High values in rotation variance occur when both or one of the end members present and form crisp boundary. Rotation in spectral fit of all template pixels is calculated as:

$$V_r = \frac{\sum_{a=0}^A (F_s(a) - F_r)^2}{A} \quad (2.4)$$

Where, A is the number of template rotation at each position.

The mean spectral variance is the average variance of the initial spectral fit obtained with equation 2.1 and is calculated as:

$$V_s = \frac{\sum_{a=0}^A V_s(a)}{A}, \quad (2.5)$$

The ratio of rotation variance in spectral fit to rotation average of spectral variance is expected to reduce non edge pixels and emphasizes crisp boundary if present since the rotation variance is high for crisp boundary.

2.2. Works done

Rotation variant template matching (RTM) since its development; is used by authors for the detection of boundaries between spectrally distinct surfaces using hyperspectral imagery. (van der Werff et al., 2007; 2006), used RTM algorithm for the detection of boundary between mineral assemblages in hydrothermal alteration systems. They have showed that the algorithm detected the selected boundaries between mineral assemblages as defined in the template. A template was designed as one dimensional image consists of 3x1 pixels and able to detect crisp and fuzzy boundaries.

In hydrothermal alteration systems, mineral assemblages are formed through hydrothermal processes. Therefore process based mapping of boundary zones between alteration facies is important for reconstructing hydrothermal process than mapping individual minerals. Supervised detection of these boundary zones using the algorithm is effective (van Ruitenbeek et al., 2006). The template is designed to consist 5x1 pixels and matched to HyMap hyperspectral imagery. (van Ruitenbeek et al., 2008) used the algorithm in the same way for detection of predefined boundaries in hydrothermal alteration zones. The algorithm used on single band image and produces a series of points that match predefined boundaries. using the RTM algorithm for the detection of boundaries in shoreline beaches using hyperspectral image. (Méndez Alves, 2007). The RTM method able to detect most of the beach boundaries expected. Other researchers used the algorithm include (Kalubandara, 2005; Oluwafemi, 2010).

2.3. Gamma ray data

Gamma ray spectroscopy provides the relative geochemical concentrations of radioelement (K, Th and U) in the upper 30-40cm of earth's crust (A.L. Jaques 1997; B.L. Dickson and Scott, 1997). Geochemical variations provide valuable information in mapping bed rock lithology, alteration, regolith materials mapping in highly weathered and vegetated terrains (A.L. Jaques 1997; B.L. Dickson and Scott, 1997; Wilfred et al., 1997). Geochemical maps define the lateral surface distribution of K, U and Th and enables in precisely locating lithological boundaries. Major variation in radioelement concentration in soils and bed rock lithology shows that there is broad lithological difference that can be mapped. While minor changes in concentration of radioelement within the unit is due to weathering and mineralizing effects. The

Lithological boundary detection using multi-sensor remote sensing imagery for geological interpretation

distribution of the three radioelement concentrations is generally follows the same trend for igneous rocks. This means that there is an increase in radioelement concentrations with increasing Si content of the rock. Shale also contains high radioelement concentration as felsic rocks (Figure 2.2) (B.L. Dickson and Scott, 1997). Concentration of radioelement in sedimentary rocks reflects parent rock and depends on the maturity of the sediments. Mature sediments have very low values while immature sediments show high radioelement content. As described by (B.L. Dickson and Scott, 1997) the concentrations of radioelement do not vary with metamorphism. However there is a wide range of values within any given rock type such that global classification of rock type based on radioelement content is not possible.

Potassium is a major constituent of the earth's crust which accounts on average of 2.35% and it occurs mainly in felsic igneous rocks as major rock forming minerals such as k-feldspars, micas and clay minerals. The concentration of potassium in mafic rock is very low and very lower in ultramafic rocks

Thorium exists in minor amount accounting in average to 12ppm of the earth's crust. The main constituents of thorium are monzonite, xenotime and zircon. These minerals are stable during weathering and remain accumulated in sand deposits (B.L. Dickson and Scott, 1997).

Uranium is also a minor constituent of the earth's crust like thorium with average abundance of 3ppm. The major Uranium bearing insoluble minerals include monzonite, xenotime and zircon. Uranium also occurs as oxides and silicate minerals such as uraninite and uraorthorite

During weathering, radio elements are released from primary mineral constituents and adsorbed on to clay, iron oxides, groundwater and organic matter. K is a mobile and soluble element under most weathering conditions and adsorbed on to clay minerals. U and Th are however less mobile than K; U associate with resistant minerals like zircon and monazite, Th is also associate with resistant minerals however acidic conditions enhance the solubility of Th. U and Th released during weathering are associated with silty fractions and sesquioxides in highly weathered profiles. K is typically high in less weathered regolith depending to the composition of bed rock and low in highly weathered regolith due to leaching (B.L. Dickson and Scott, 1997; Wilford and Minty, 2006).

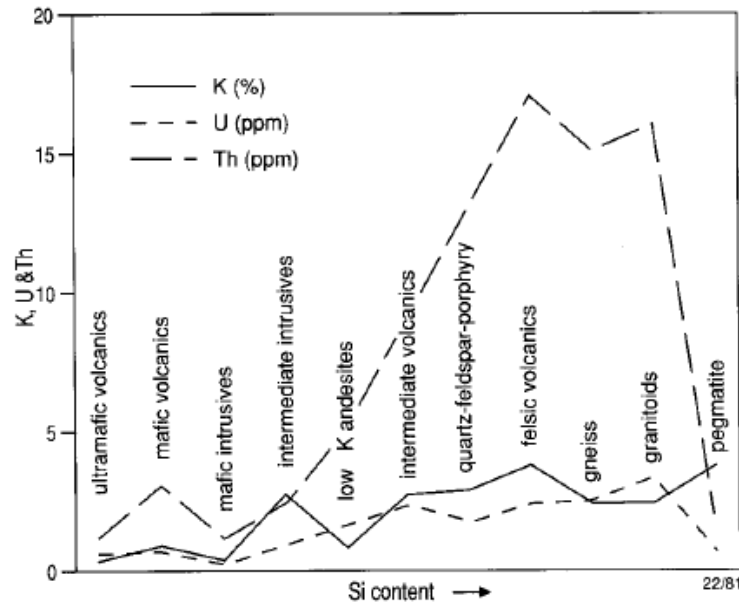


Figure 2-2: Variation in average K, Th & U content in igneous rocks with increasing Si content (B.L. Dickson & Scott, 1997)

2.4. Magnetic data

Aeromagnetic surveys record anomalies in shallow and deeper depths which are related to host rock with magnetic minerals (Shufelt, 2000). Aeromagnetic anomalies are related geological features; structures, magnetic susceptibility of rocks. The analytical signal calculates the signal of a channel it can be used in locating edges of remanently magnetized bodies in areas of low magnetic latitude. The analytical signal positions anomalies above the source of the body and also suppresses sources from depth by emphasising shallow sources which is the importance for lithological contact mapping.

2.5. ASTER

ASTER imaging spectroscopy acquires spectral reflectance of ground materials in contiguous narrow spectral bands on electromagnetic spectrum. three bands between 0.52-0.86 in visible near infrared (VNIR), six bands from 1.6-2.43 μm in shortwave infrared (SWIR) and five bands from 8.125-11.65 μm in thermal infrared (TIR) with 15, 30m and 90m resolution respectively (Hewson et al., 2005). Most of the information for geological mapping is acquired in the VNIR to SWIR (0.4- 2.5 μm) regions of electromagnetic spectrum. VNIR bands provide information on transition metals, rare earth elements and vegetation cover. The SWIR wavelength provides information on carbonates, hydrates and hydroxide minerals (Rowan and Mars, 2003).

Band rationing is a powerful technique for enhancing the compositional variation of surface materials by suppressing differences in albedo and topographic effects (Gad and Kusky, 2007). Ratio images from SWIR wave lengths are useful for the discrimination of lithological units. However presence of vegetation cover affects the remote sensing detection for the discrimination and mapping of lithological units.

3. STUDY AREA

3.1. Location

The study area is located in south-central Uganda; Kiboga bounded by 31°30' and 32°00' longitude and 0°30' and 1°00' latitude which cover 55 x 55 km² area Fig (3.1)

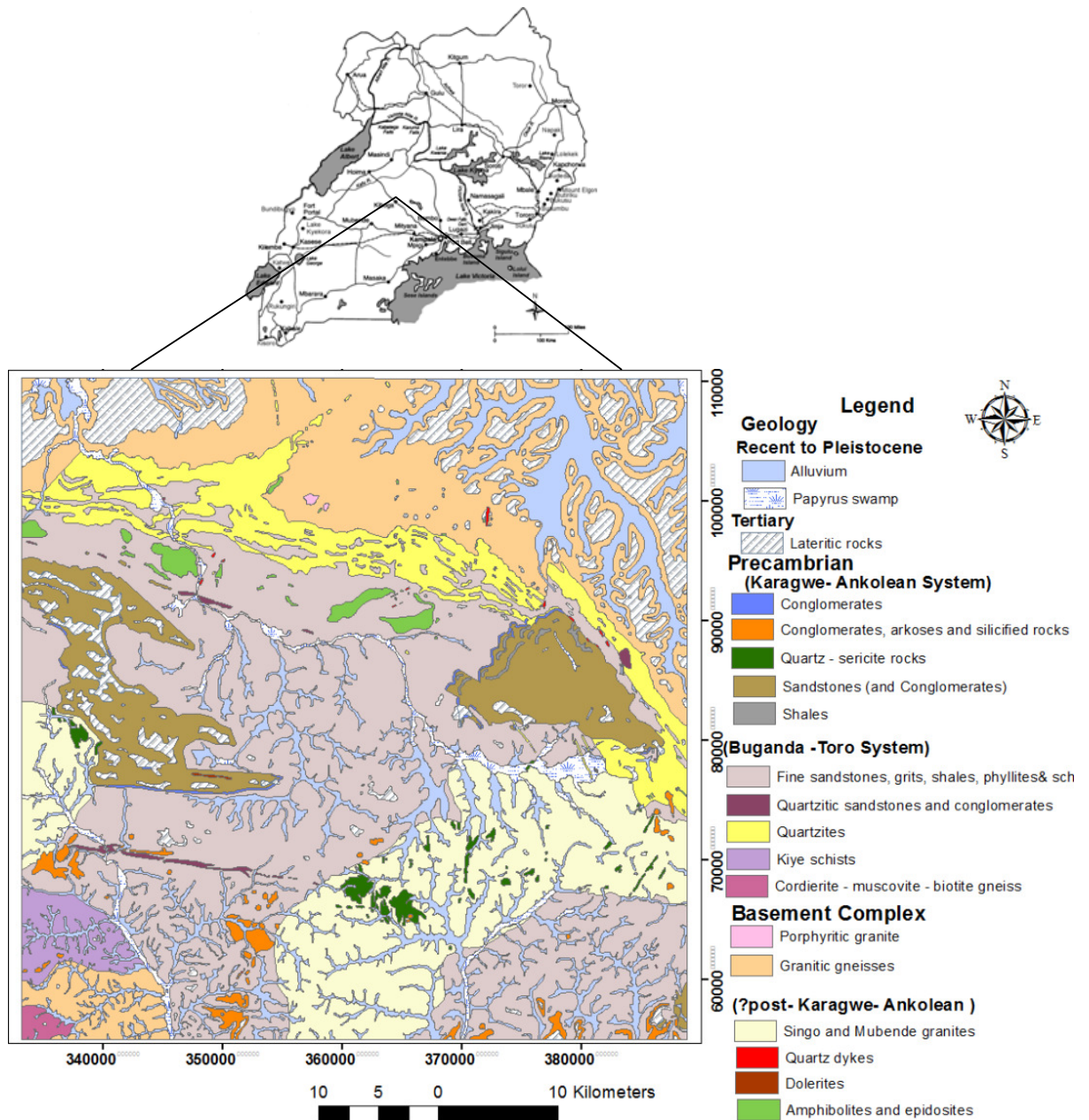


Figure 3-1: Location of study area, source , (R.J. Johnson and Williams, 1961)

3.1.1. Regional geology

The geology of Uganda comprises mostly Archean gneissic- granulitic complex rocks and Proterozoic metasedimentary rocks. The Archean Gneissic- Granulite complex rocks regarded as basement are exposed in the northern and south central parts of the country. The Granulite rocks are highly metamorphosed during the middle Archean (Watian event) period and occur in the northern and western parts of Uganda. Rock types include acid and intermediate granulites and quartz diorite, quartz- feldspatic rocks. During the late Archean (Aruan event) period granitic and biotitic rocks were formed by retrograde metamorphism of granulite facies assemblage and these rocks are exposed in the northern and south central part. There are three suits of supracrustal rocks formed in Uganda during Proterozoic age. In the first phase; rifting occurred across the southern Uganda during early Proterozoic that isolated Uganda from Tanzania. As a result of this tectonic event; Buganda-Toro system (Rwenzori Fold Belt) rocks such as Phyllites, quartzites, schists, and gneisses are formed by low to medium metamorphism of volcanic and clastic sedimentary infill and associated weathering of adjacent cratons. Metamorphic grade generally increases from east to west where uplifted schists and gneiss form the Rwenzori Mountains. The Buganda-Toro system rocks are exposed in eastern, southwestern and central part of Uganda. The second phase of Proterozoic tectonism is associated with continental rifting of kibaran orogeny (1800- 1400Ma). The Kibarian orogeny extends from southwestern Uganda, through northwestern Tanzania, Rwanda, Burundi into the Democratic Republic of Congo. The Karagwe- Ankolean system is formed during this orogeny and is composed of gneiss, migmatites, folded metasediments, conglomerates and volcanic sequences. The final phase of Precambrian tectonic event in Uganda is related to the collision of east and west Gondwana which forms Mozambique mobile belt. The mobile belt is recognized in Uganda as the Karasuk group of metasedimentary rocks over thrust onto Aruan gneisses. Tertiary to Cenozoic sedimentary and volcanic rocks occur in the down- faulted western rift valley. There exists minor Tertiary to recent sediments and volcanics which occur along the eastern and western borders in the rift systems (Schluter, 2006).

3.1.2. Local geology

The geology of the area comprises basement rocks of Archean age, Precambrian rocks and minor recent deposits. Granitic gneiss is the oldest basement rock found in the north of the study area. This unit is highly weathered and overlain in the North east part by swamp and alluvial deposits. The quartzite, fine sandstone, Phyllites, slate, siltstones and shale of Buganda-Toro series were laid down on eroded surfaces of the basement complex rocks and were subsequently folded and metamorphosed. Amphibolites and epidote found as patches associated with fine sandstone, schist, Phyllites and slates in the northern part close to the quartzite ridge. Amphibolites belong to dolerite sills which have been altered during the folding and metamorphism of the Buganda series. The rocks of the singo series (Karagwe- Ankolean system) form the Bulaga and Butologo Plato in the east and west part of the area deposited following the folding and metamorphism of Buganda series. These rocks consist of sandstones and conglomerates and some shale and have been subjected to tensional faulting. The Singo and Mubende batholiths are intrusive in the Buganda series with sharply defined cross cutting contacts. The mityana serious which consists of conglomerates, arkoses, sandstones and silicified rocks were subsequently laid down on the Buganda series rocks (Nyakairu et al., 2002; R.J. Johnson and Williams, 1961 and Schluter, 2006).

4. MATERIALS AND METHODS

4.1. Materials

Data set used for the study include

- 1: 100,000 geological map of Kiboga published by Geological Survey of Uganda in 1960.
- Remote sensing data: ASTER image and DEM
- Geophysical data: gamma ray and aeromagnetic (analytical signal)
- Field observations

The high resolution geophysical data are acquired by FUGURO, REF: FCR2417A, for the ministry of energy and mineral development of republic of Uganda in 2007. Table 4.1 shows survey specification of FUGRO data acquisition. Both gamma ray and magnetic data are gridded at 50m resolution. ASTER scenes acquired in 2008 and DEM were obtained from ITC.

Table 4-1: Survey Specifications of FUGRO data acquisition

Magnetic Data Recording Interval	0.1 seconds
Radiometric Data Recording Interval	1 second
Radiometric Data Recording Interval	80 meters
Flight Line Spacing	200 meters
Tie Line Spacing	2000 meters
Flight Line Trend	035 degrees
Tie Line Trend	125 degrees

4.2. Software

- Envi version 4.7 including template matching algorithm
- Envi2 tools for edge detection
- ERDAS imagine 10 ,
- ArcGIS 10 and
- Oasis Montaj

4.3. Methods

The methodology of this study is based on the objectives formulated in section 1.3. Figure 4.1 shows the methods and general workflow of this research.

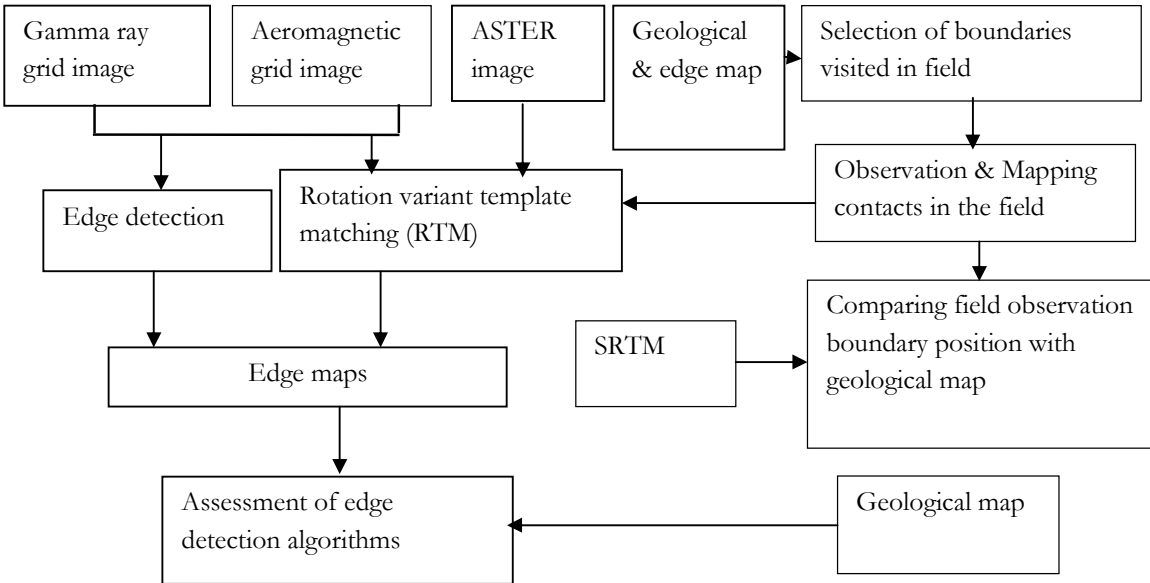


Figure 4-1: General workflow of the methods used

4.3.1. Preparation for field work

Preparation and field work planning have been done in order to select contacts to visit and characterize in the field. For this purpose; edge detection was done on Thorium, Uranium and Potassium grid maps. The edge map along with published geological map was used for selecting the contact to be visited and to plan the field traverses. The boundaries between gneissic granite- quartzite and granite- sandstone (this sandstone unit comprises of different rocks and named as “fine grained sandstone, grit, shale, Phyllites and schist”) were selected and field traverses were planned in these areas.

4.3.2. Field observations

The field work was carried out from 12 to 25 September 2010 in south central Uganda, Kiboga area. Areas in the north and southeast of the study area were visited to characterize and map the boundary zones between granitic gneiss- quartzite and granite- sandstone respectively. GPS readings were taken along the traverses on both sides of the boundary zone in areas that are accessible (Figure 4.2). Figure 4.3 shows picture of quartzite unit. Field observation records are found in the appendix.

Lithological boundary detection using multi-sensor remote sensing imagery for geological interpretation

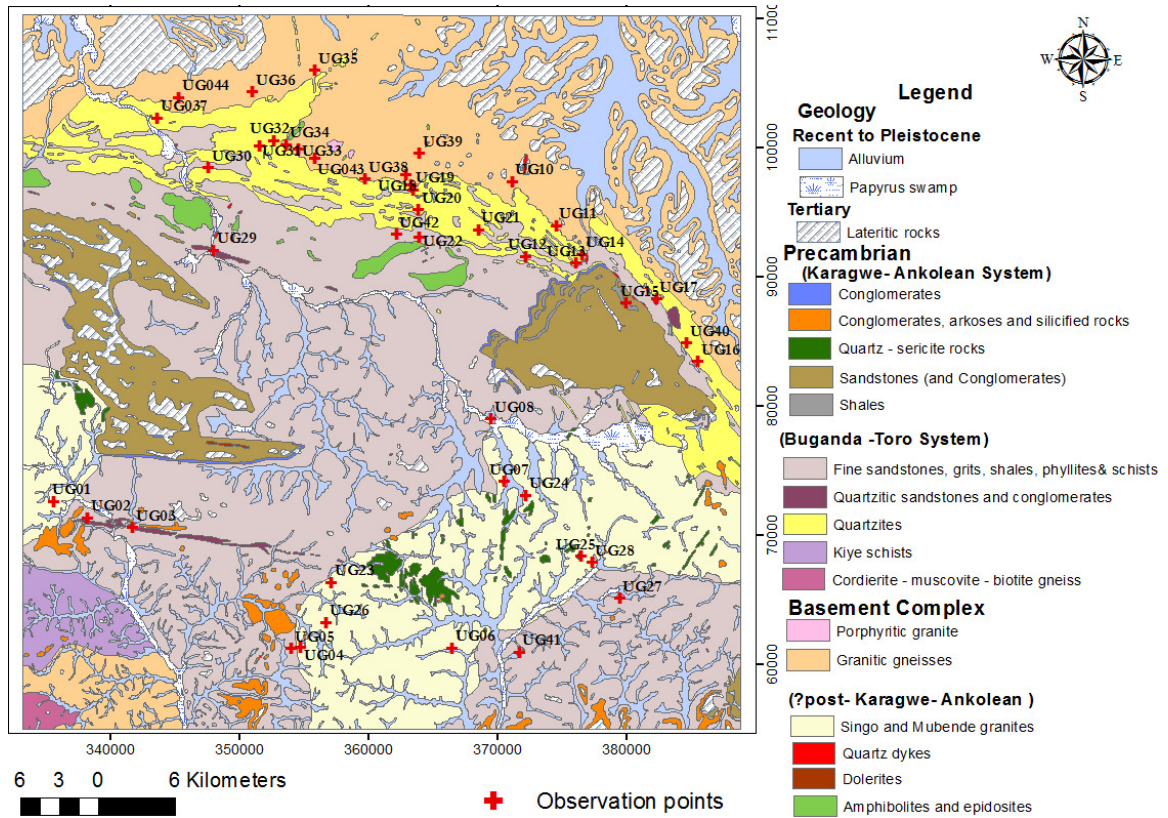


Figure 4-2: Field observation location points



Figure 4-3: Quartzite unite, picture taken looking to the east from gneiss side

4.3.3. Image pre processing

As mentioned in section 4.1 gridded gamma ray images are obtained. This grid images are transformed to concentration values in order to get the variations of radioelement concentration on the units of interest. This is helpful in the determination of end member selection for template matching. Moreover; individual layers of radioelement (Potassium, Thorium and Uranium) images are scaled to have the same range of values when these images are stack to use multiple layers.

ASTER scenes covering the area are projected to UTM zone 36N projection using WGS84 datum. These scenes are stacked and subset to the study area then a mosaic was generated from the subset image. SWIR bands of ASTER image were resampled to VINIR pixel size to a spatial resolution of 15 m. Band ratio was calculated from the SWIR bands.

4.3.4. Methods to apply edge detection algorithms

Edge detection and rotation variant template matching algorithms (RTM) are used for the detection of boundaries between granitic gneiss-quartzite (b1) and sandstone–granite (b2).

Edge detection

Hyperspectral Laplace gradient filtering in all direction using Euclidean distance measure used for the detection of lithological boundaries. It combines both XY and diagonal gradients directions. These gradient measures are combined with averaging the differences of the central pixels with its eight neighbouring pixels (Bakker and Schmidt, 2002).

Rotation variant template matching (RTM)

As mentioned in previous sections and also at the beginning of this section the algorithm is used in this research for the detection of boundaries between lithological units. The boundary between two rock units is determined by the variation of mineral assemblages contained in them.

Template dimension of 5x1 pixels and spectral matching method Euclidean distance measure are used for detection of boundaries between gneiss-quartzite and sandstone-granite. End members are taken by defining the region of interest (ROI) at different lithology as shown in figure 4.4. The roi's are defined in such a way that variation in spectral signatures for the different lithology also the location of roi's taken from around field observations to insure the signature related to our interest signature. This means that the roi's taken correspond to the units of interest as verified in the field. In case of thorium and Uranium; the variation on the pair of lithological units show distinct spectral signatures .definition of roi's systematically applied for all images.

The algorithm is applied to single radioelement images first and then multiple layers of these images were used to see whether using multiple layers increases the quality of matching result in identifying those boundaries or not. So that potassium, Thorium and Uranium images were used separately and then stacked Thorium-Uranium, Thorium-potassium and Potassium-Thorium-Uranium images were used. Analytical signal of magnetic data was used as single band image. The created band ratio from the SWER region of ASTER image combined as colour composite RGB (4/5, 4/6, 4/7) was used.

The results of RTM for each input image is presented by combining three output measures in RGB colour composite. From the derived measurements; optimal template fit, rotation variance and mean spectral variance could be used for the detection of boundary between spectrally contrasting signatures Since ratio of rotation variance and mean spectral variance is expected to reduce false edges; hence ratio of these measures, optimal template fit and rotation average of spectral variance are used as RGB colour composite respectively.

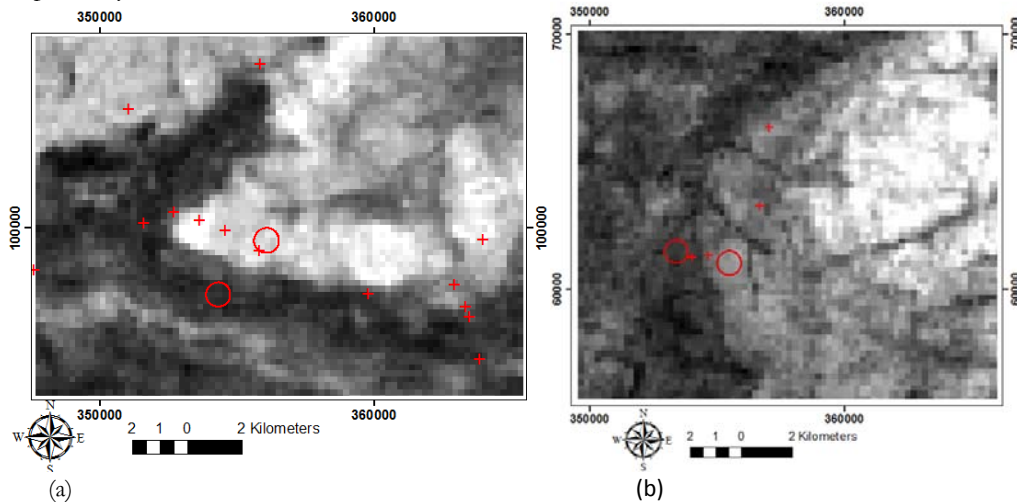


Figure 4-4: Showing areas where roi's defined for template design on thorium images. Red circles are areas where roi's defined for the template design for boundary between gneiss and quartzite and (a) for sandstone and granite (b). The red plus signs are observation points

5. RESULTS AND DISCUSSION

5.1. Lithological boundaries determined in the field

In the northern study area, quartzite forms a series of prominent ridges which trends in NW- SE direction. The ridge usually appears with gentle slopes at the bottom and becomes steeper on the top. Vegetation is sparse and it is resistant to weathering, and appears to be bare contrary to the surrounding units. The granitic gneiss forms relatively flat and low topography with few rock exposures due to weathering. In some places it is exposed as boulders towards the contact zone with quartzite.

In southern area, both the granite and sandstone are dissected by swamp and river channels that form undulating surfaces. Weathered exposures of granite boulders observed close to the boundary with sandstone. The sandstone is also highly weathered and rock exposures are hardly found.

Some field observation points were used to create profile lines across the boundary for the description of boundary (Figure 5.1). Four profile lines were produced across granitic gneiss (Figure 5.2) and quartz boundary and two across sandstone and granite boundary (Figure 5.3).

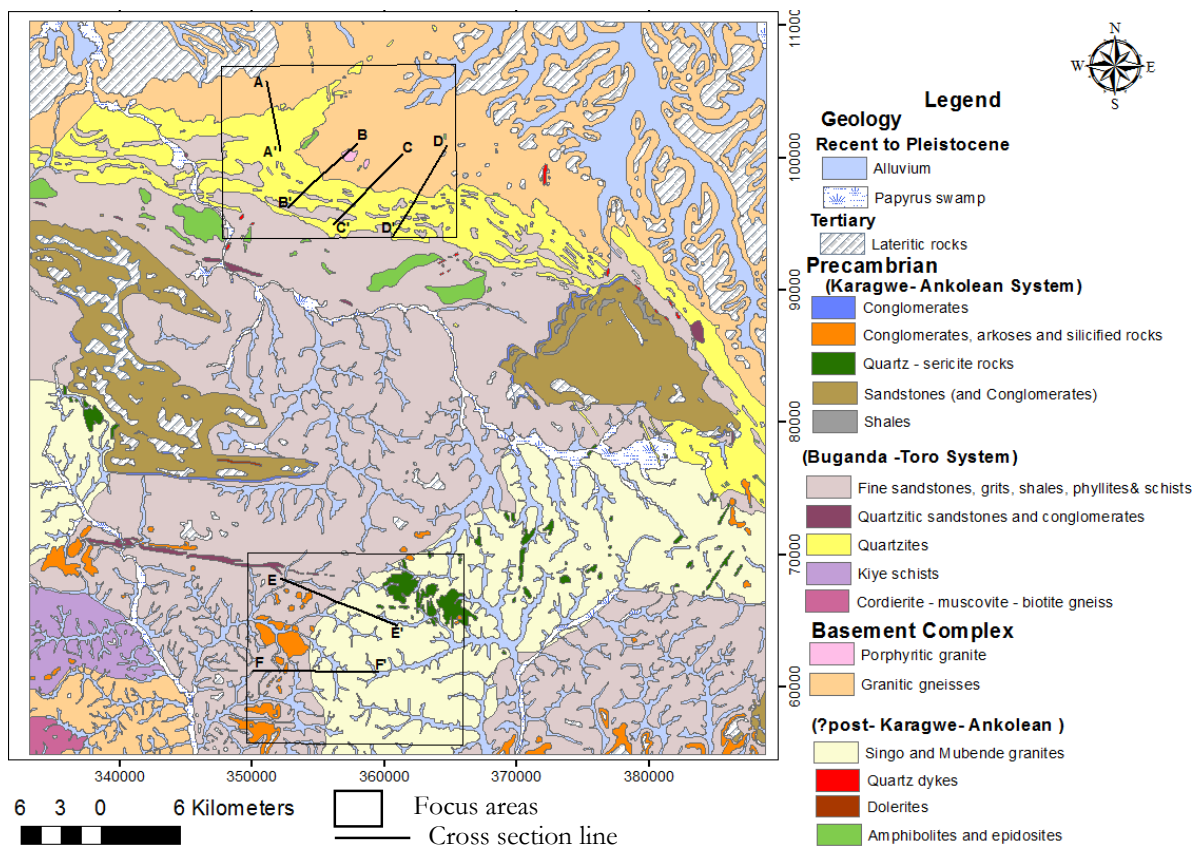


Figure 5-1: Selected cross section lines produced across boundaries at some field observation points

Figure 5.2 shows the four profiles produced across boundary between granitic gneiss and quartzite. It shows the field estimated boundary locations in relation to geological map.

Along profile AA' exposure of weathered granite gneiss boulders observed closer to quartzite. Quartzite unit forms lower topography towards the contact with the gneiss. The boundary zone is estimated close to

Lithological boundary detection using multi-sensor remote sensing imagery for geological interpretation

the resistant quartzite ridge. Along profile BB', the gneiss unit forms relatively low topography which increases towards the quartzite unit. It forms local hills that end at the bottom slope of quartzite ridge. The boundary zone is estimated at the low laying area (valley) usually characterized by dense vegetation. Along profile CC' the granitic gneiss unit forms flat surface that extends to high elevation towards the quartzite. Rock exposure is hardly found due to weathering. Weathered boulders of gneiss exposed near the bottom slope of quartzite ridge. Location of the boundary along this profile is estimated close slope break of quartzite ridge which forms steep slope. Along profile DD' the low laying area is covered by weathered material and dense vegetation. Rock exposures couldn't found along this profile. The boundary zone is estimated at the bottom slope of resistant quartzite ridge. The quartzite ridge gently slopes at the bottom and becomes steeper on top.

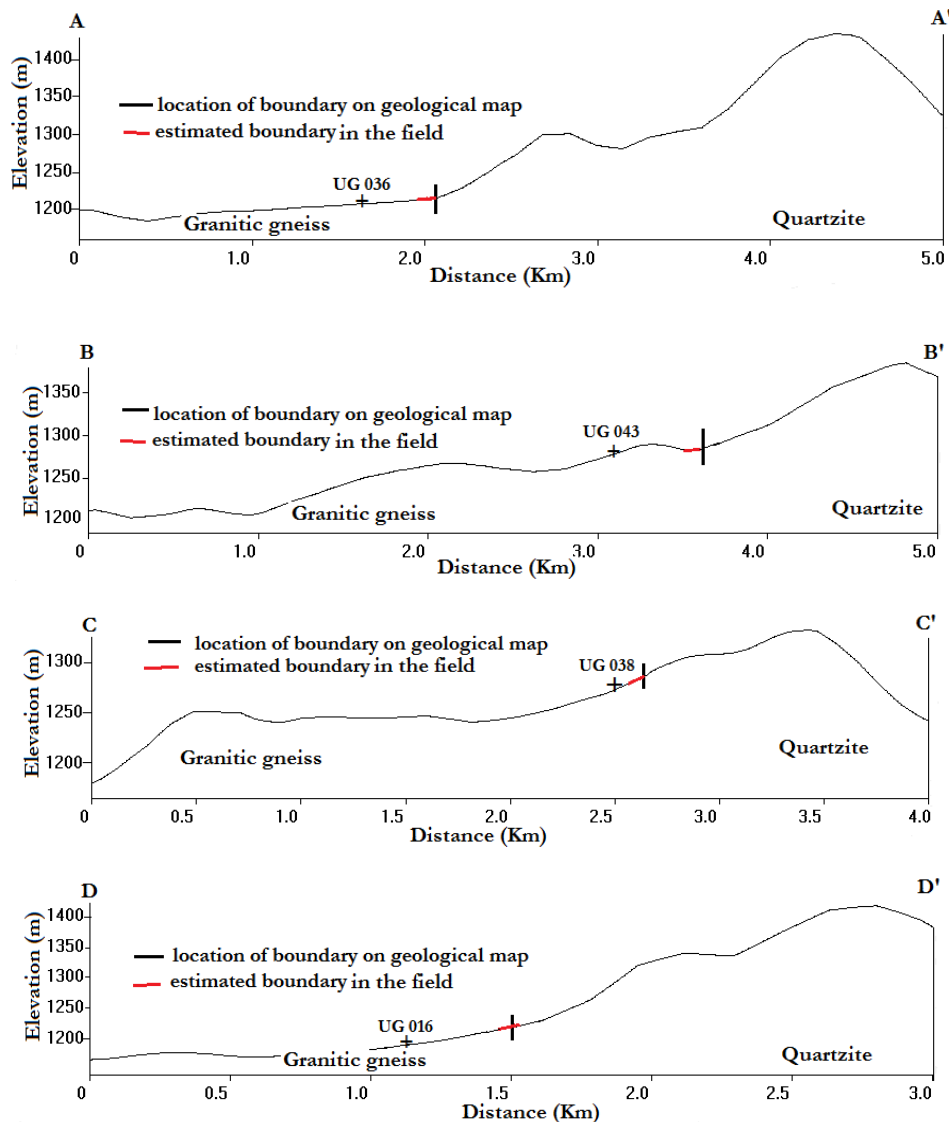


Figure 5-2: Profiles across boundary between granitic gneiss and quartzite. It shows the location of estimated boundary zone from field observations in relation to elevation and rock units.

Figure 5.3 shows the four profiles produced across boundary between sandstone and granite. It shows the field estimated boundary location in relation to geological map

Lithological boundary detection using multi-sensor remote sensing imagery for geological interpretation

Along profiles EE' and FF', both the sandstone and granite forms local hills which are cut by swamps and form low lying area in between. The low lying area covered by swamps and alluvial channels seems to follow the boundary between the units along these profiles. Exposures of weathered rocks on both sides of the boundary are observed along profile FF'.

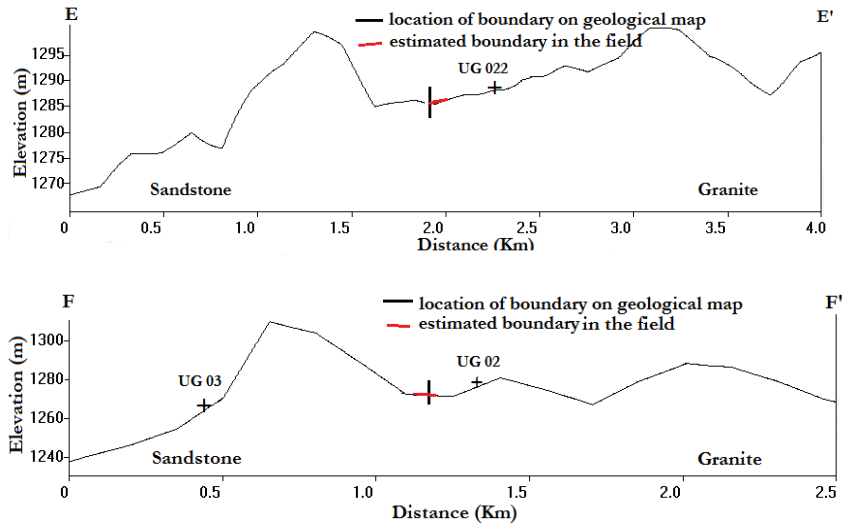


Figure 5-3 : Profiles across boundary between sandstone and granite. It shows the location of estimated boundary from field observations in relation to elevation and rock units.

Along the profiles, the boundary on geological map coincides with the determined boundary from field observations at places. It was observed that the determined boundary in field mostly deviate from boundary on geological map as shown along profiles AA', BB', CC' and EE'. Only show coincidence along profiles DD' and FF'. lithological contact mapping based on field observation points couldn't give the actual position due to the fact that geological units are covered. As it was mentioned earlier the study area is covered by vegetation and weathering material, locating the exact position of the boundary on the field was not possible and only approximate estimation could be made at places. It is also important to consider that interpretation of the location of boundaries on published geological map could be influenced by interpreter.

5.2. Processed image subsets

The processed images were subsets to focus at boundary location; Figure 5.4 shows image subsets to focus on boundary between granitic gneiss and quartzite and figure 5.5 shows images subset to boundary between sandstone and granite.

Lithological boundary detection using multi-sensor remote sensing imagery for geological interpretation

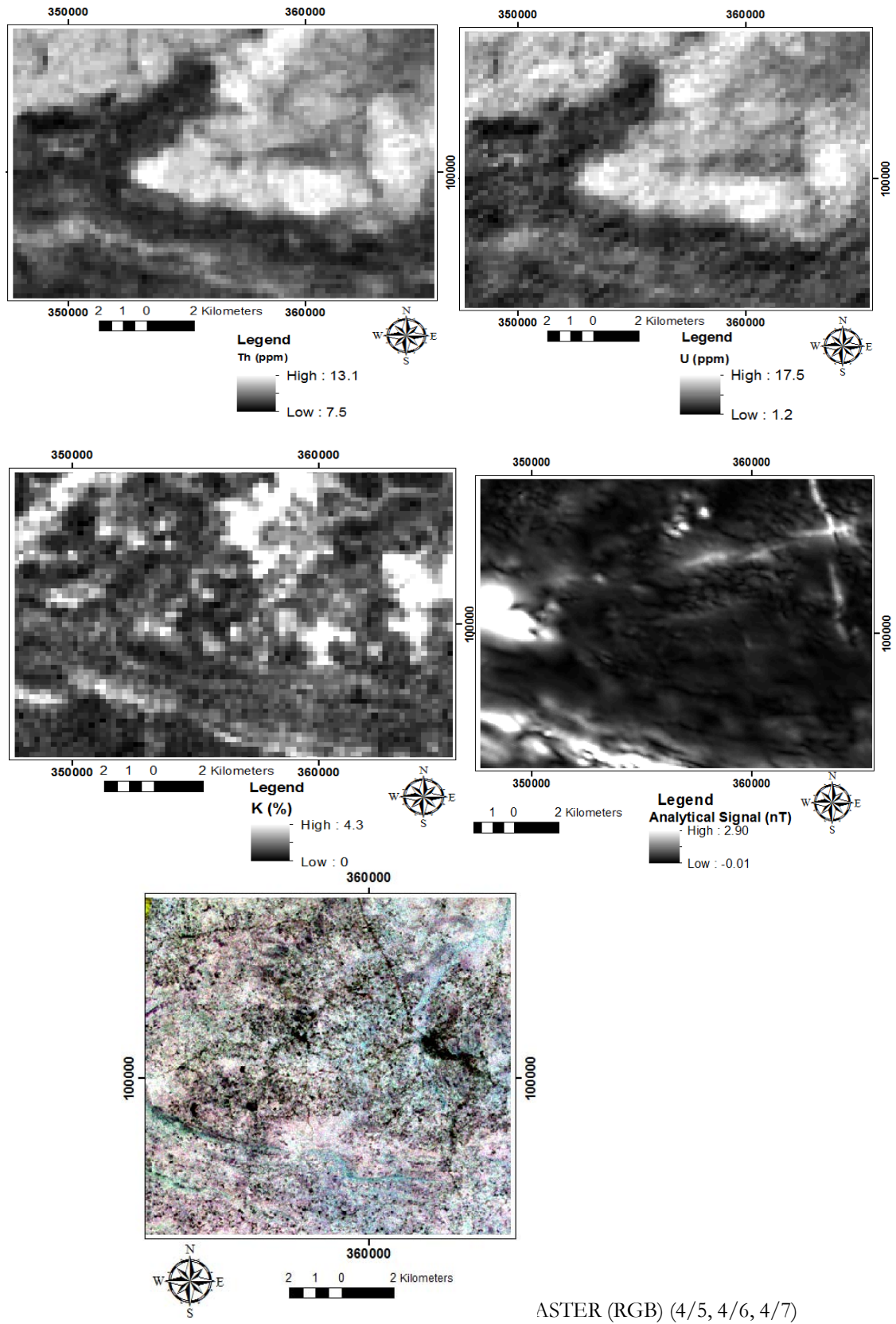


Figure 5-4: Processed images subset to focus on boundary between granitic gneiss and quartzite

Lithological boundary detection using multi-sensor remote sensing imagery for geological interpretation

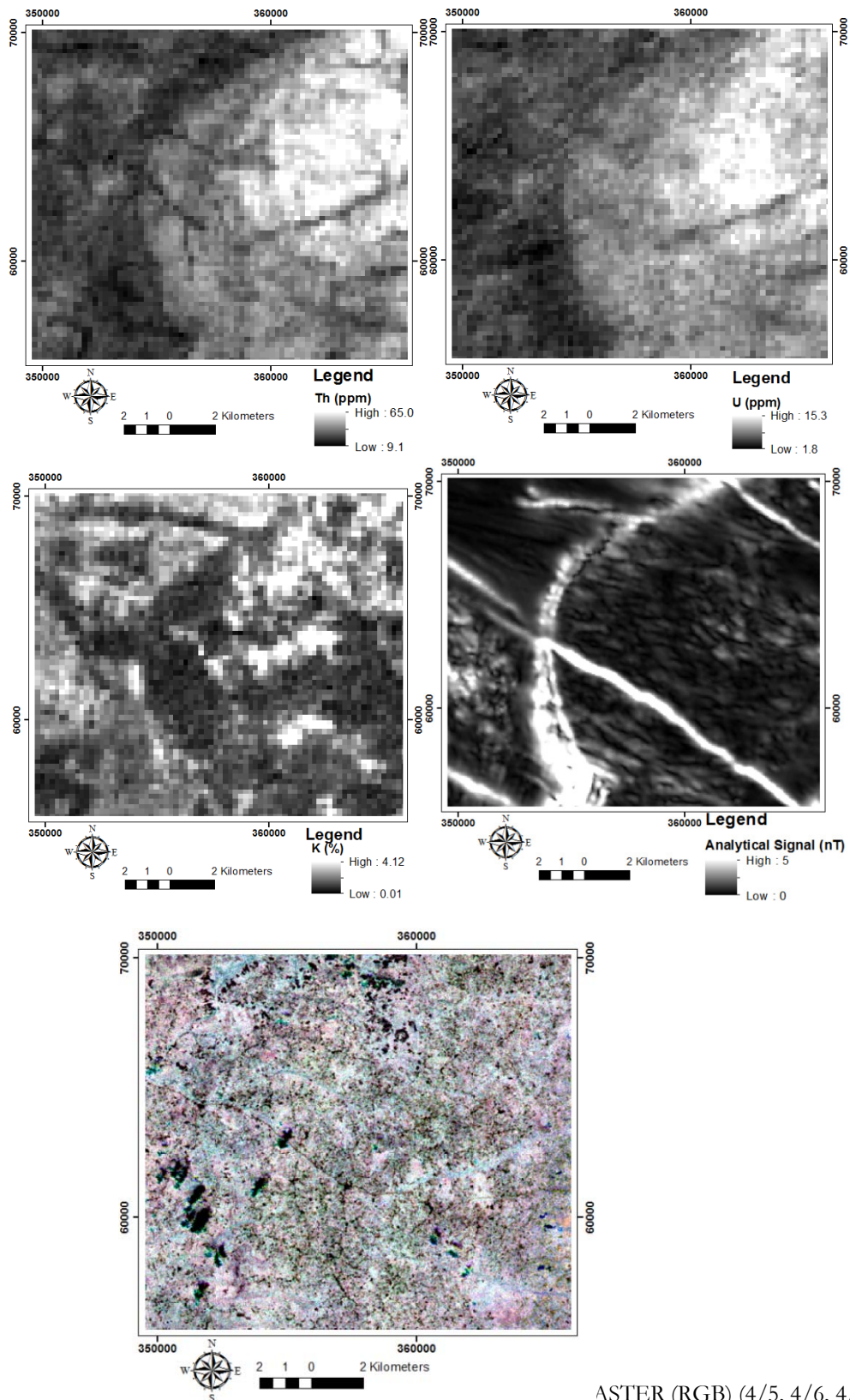


Figure 5-5: Processed images subset to focus on boundary between sandstone and granite

5.3. Edge detection

Edge detection results using single and multiple radioelement images are presented at the beginning, and then results from magnetic images follow.

5.3.1. Applied to gamma ray spectrometry

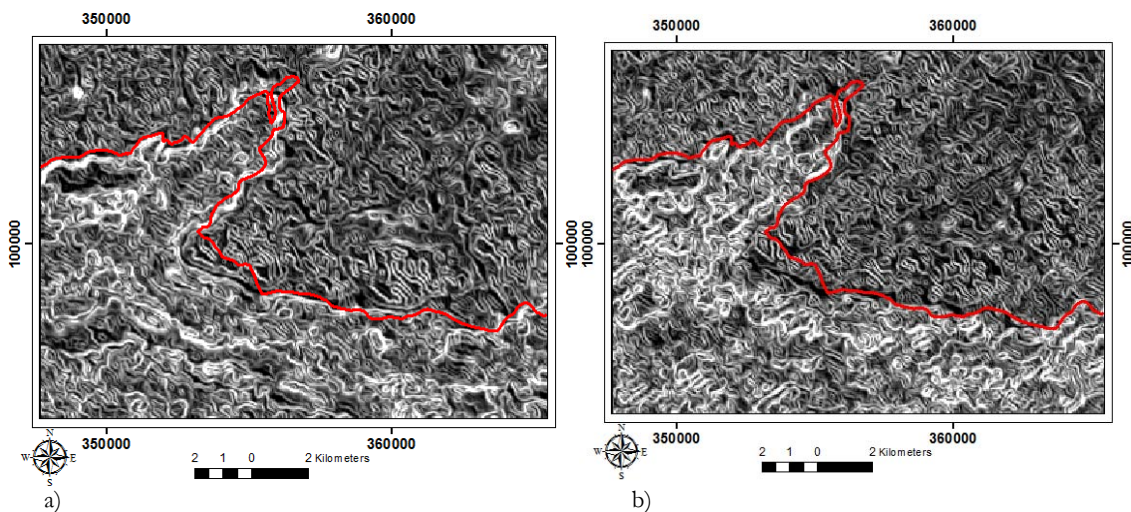
Figure 5.6 shows edge maps produced from different input layers for the detection of boundary between granitic gneiss and quartzite (b1). Among the single input layers thorium and uranium show the location of boundary as can be recognized from the edge images (Figure. 5.6a & b); though it does not show any pattern when potassium image used as shown in figure 5.6c. In Figure (5.6a & b) the gneiss unit is seen as less bright pixels and quartzite unit with bright pixels. The edge map produced using thorium-uranium image give similar response as using single thorium or uranium image (Figure 5.6d). However the edge map obtained using potassium-thorium and potassium-thorium-uranium stack images (Figure 5.6 e & f) do not show clear response for the presence of boundary.

Similar response is obtained for the detection of boundary between sandstone and granite (b2) using the same data layers (Figure 5.7).

Visual interpretation of the results from all input images appears to have more edge pixels. The edge maps produced show two spectrally contrasting regions in the image. These two contrasting regions are characterized by bright and dark pixel area in the image indicating relatively edges (differences in Euclidean distance between pixels) and local homogeneity respectively.

Results obtained using thorium, uranium and thorium- uranium images for both boundaries (Figure. (5.6a, b & d) and Figure (5.7a, b & d) show areas with high variability and local homogeneity indicating the presence of contrasting signatures. From these observations the boundary zone in the edge maps could be located at the transition from brighter areas to less bright ones. The input images used in this case show spectral variations on the pair of rock units indicating the presence of boundary. For example thorium have high and low concentration values on gneiss and quartzite respectively, thus the edge filters able to measure the local variability in the image giving low and high values.

Both boundaries are not as much detected on thorium-uranium-potassium as shown in (Figure (5. 7f) & Figure (5.7f)). Also results obtained from potassium and thorium-potassium on both boundaries show more edge pixels throughout (Figure (5.6c & e) and Figure (5.7c & e)). This could be because potassium does not give distinct spectral variations on the lithological units considered.



Lithological boundary detection using multi-sensor remote sensing imagery for geological interpretation

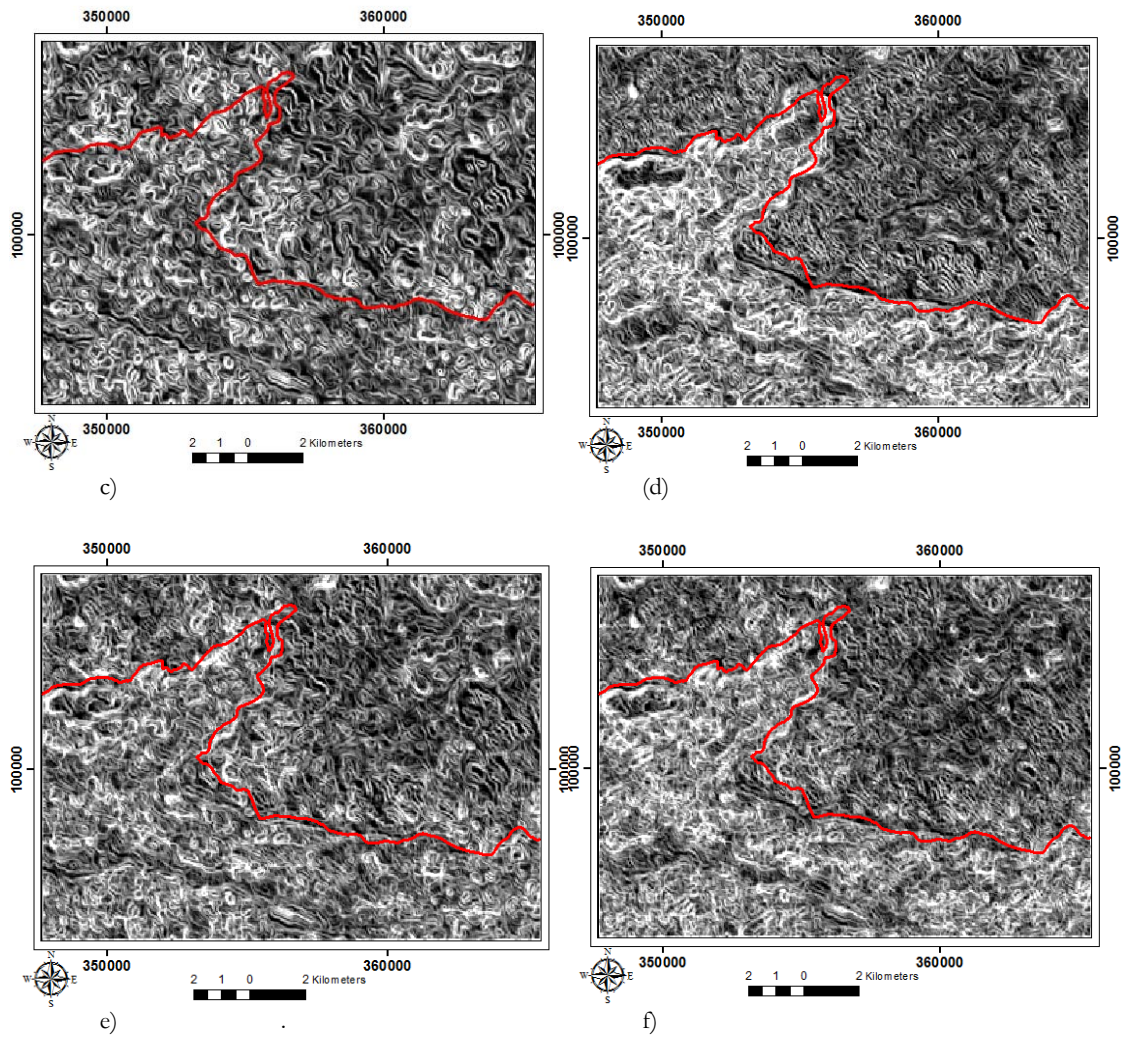
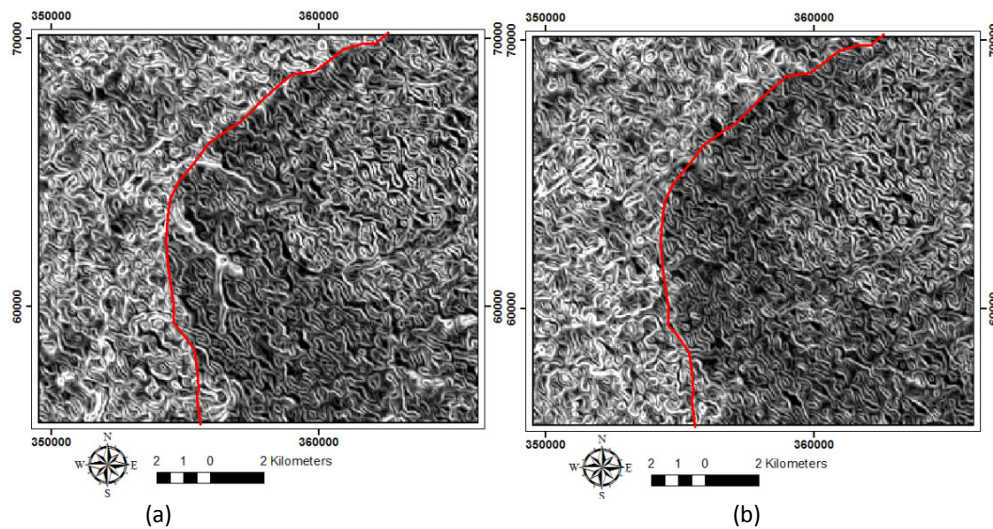


Figure 5-6: Edge maps produced from a) thorium, b) uranium, c) potassium, d) thorium-uranium, e) potassium-thorium and f) potassium-thorium-uranium images. The red line indicates the position of boundary between granitic gneiss and quartzite on geological map



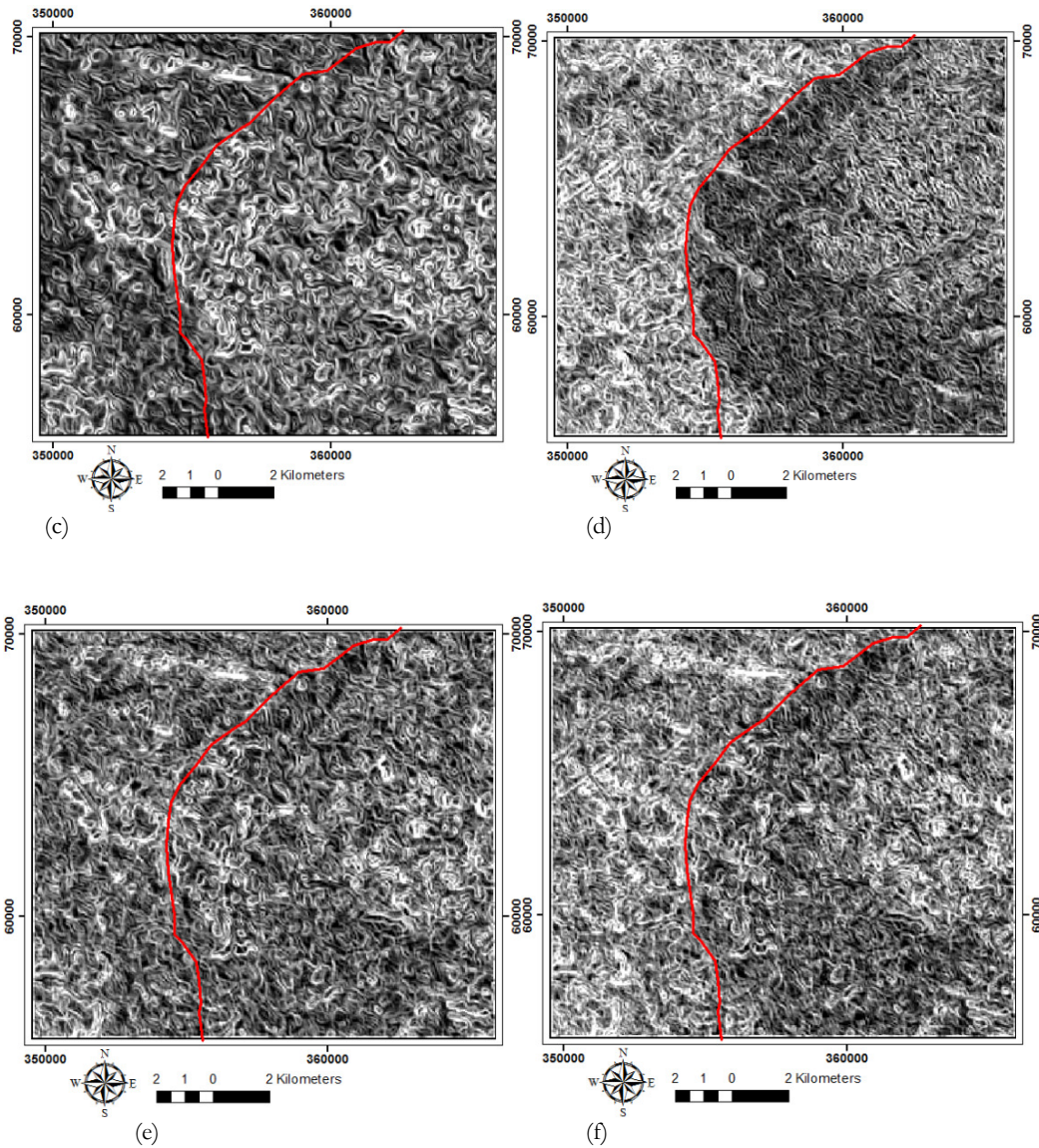
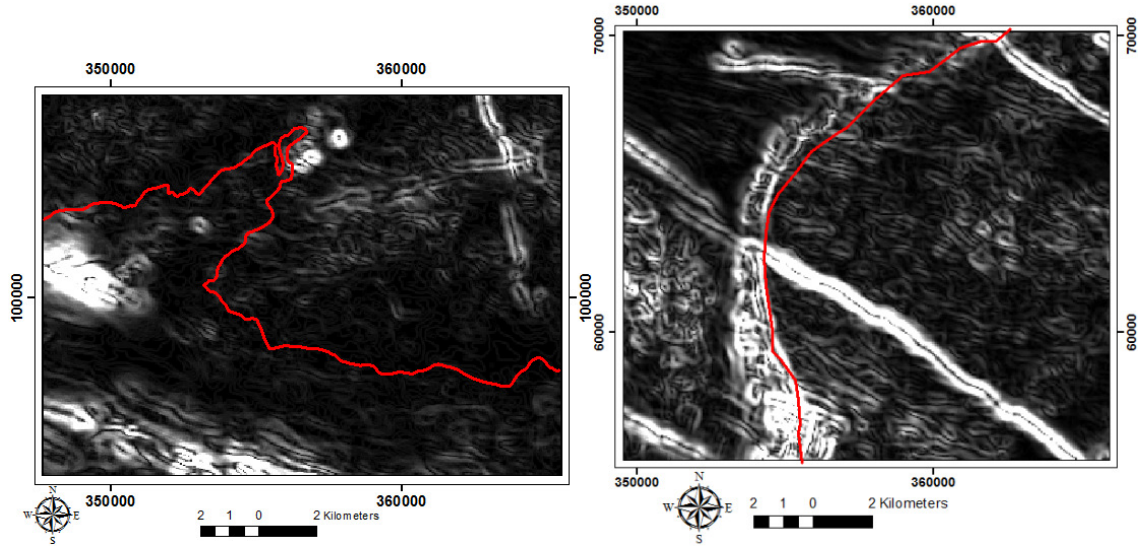


Figure 5-7: Edge images produced from a) thorium, b) uranium, c) potassium, d) thorium-uranium, e) potassium-thorium and f) potassium-thorium-uranium images. The red line indicates the position of boundary between sandstone and granite on geological map

5.3.2. Applied to Analytical signal of total magnetic intensity

Edge map of analytical signal image is shown in (Figure (5.8)). Most of the edges identified in this image are related to magnetic contacts found in sub surfaces. Bright areas represented by magnetic high and dark one are none. From Figure (5.8b), the edge of magnetic anomaly follows the edge of the granite body and seems to coincide on one side with the boundary between granite and sandstone. Other elongate bright pixels cut through the rocks are related to structural features in sub surface. There is no indication of presence of boundary in Figure 5.8a.



a) Gneiss-Quartzite

b) Sandstone-Granite

Figure 5-8: Edge maps produced from analytical signal of total magnetic intensity image

5.4. RTM template matching

In this section results obtained using gamma ray images will be presented first and the results obtained using magnetic and ASTER follow.

5.4.1. Applied to gamma ray spectrometry

Figure 5.9 shows template match results obtained using single and multiple layers of radioelement images for the detection of b1. Good matching result are obtained in all outputs and presented by red lines. The red lines show optimal template fit which present in all contrasting signatures used in the design of the template if present. The boundary is clearly indicated by a continuous red line running in west- east direction on most of the images except potassium. In addition several positive matches are observed in the entire image where some of them enclose lithological units. From Figure (5.9a), shown match pixels forming similar boundary in the south of the area. The same area in Figure (5.9b) shows more disconnected and smaller polygons. Figure (5.9d) shows the result when these layers are stack together and it shows less scattered match pixels and well-connected clear boundary pixels in the south area. The results from the stack images with potassium (Figure5.9e & f) shows more scattered match pixels and those which form boundary do not come out clearly as compared to results from single image. Result obtained using potassium does not show the boundary considered even though positive match pixels are present (Figure 5.9c).

Lithological boundary detection using multi-sensor remote sensing imagery for geological interpretation

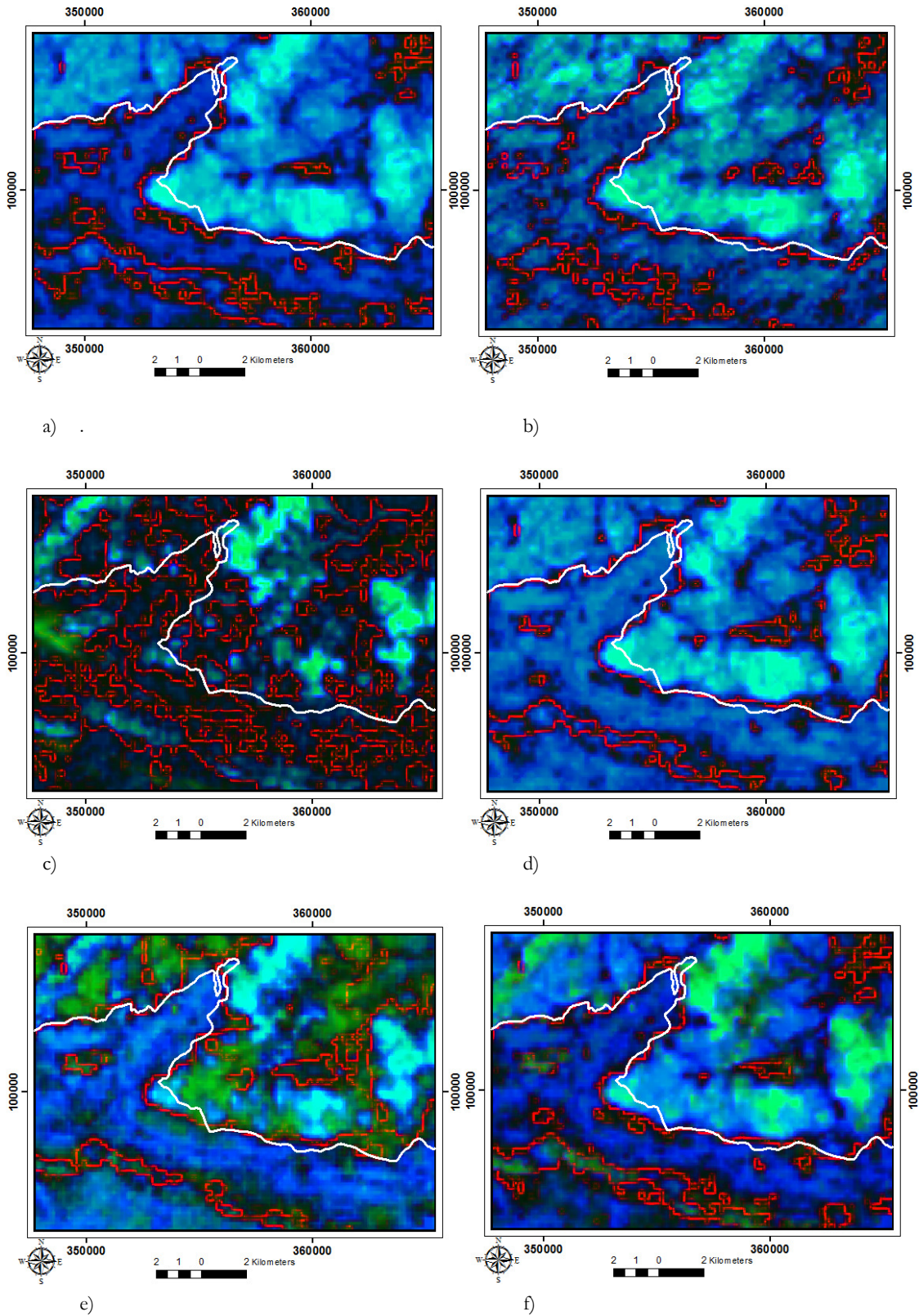


Figure 5-9: Template matching results of a)thorium, b) uranium, c) potassium, d) thorium-uranium, e) potassium-thorium and f)potassium-thorium-uranium for boundary between gneiss and quartzite. the white line indicates the position of boundary on geological map

Lithological boundary detection using multi-sensor remote sensing imagery for geological interpretation

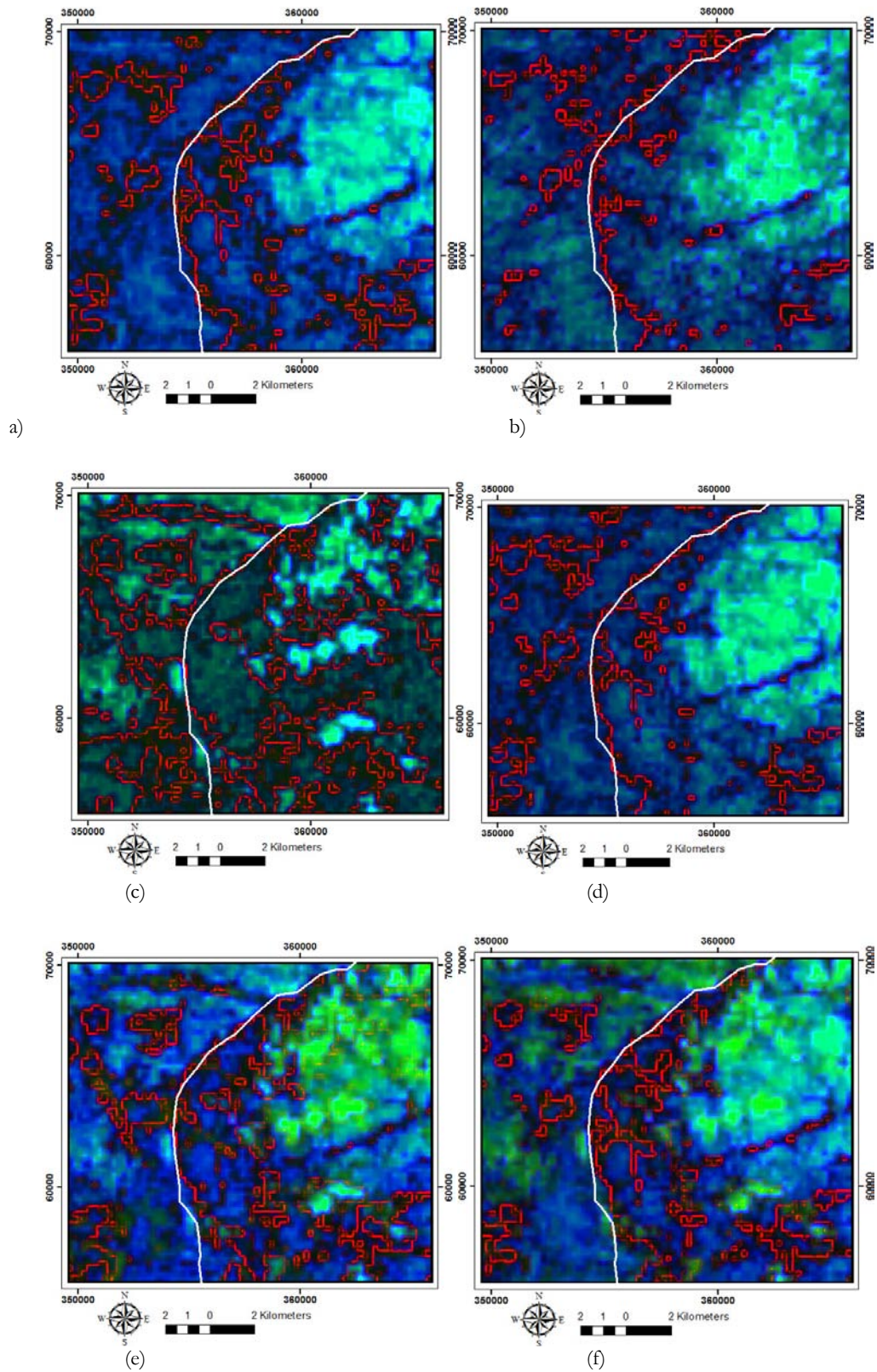


Figure 5-10: Template matching results of a) thorium, b) uranium, c) potassium, d) thorium-uranium, e) potassium-thorium and f) potassium-thorium-uranium for boundary between sandstone and granite. The white line indicates the position of boundary on geological map

Lithological boundary detection using multi-sensor remote sensing imagery for geological interpretation

Template matching results for the detection of b2 using same images as previous are shown in Figure 5.10. High matches are again present in all outputs and indicated by red line signifying the presence of both contrasting signatures. The boundary is well detected again on thorium, uranium and thorium-uranium images indicated by a nice red line running north south as shown in Figure 5.10a & b & d respectively

Figure 5.10c shows the result obtained using potassium; which shows many match pixels indicated by red line in the entire map. However the boundary between sand stone and granite is not indicated. The boundary is not as much detected on the stack images of thorium-potassium and thorium-uranium-potassium (Figure 5.10e & f)

The RTM algorithm able to detect lithological contacts as designed in the template. Both boundaries b1 and b2 are well detected using thorium, uranium and thorium-uranium images as shown in Figures 5.9a, b & d and Figure 5.10a, b & d respectively. b1 is also detected on thorium-potassium and thorium-uranium-potassium images. The results obtained are related to the input layers which are used in the design of the template. Thorium and uranium show significant variations in the pair of rocks considered (granitic gneiss-quartzite and sandstone-granite). This means that considering granitic gneiss and quartzite for example, thorium and/or uranium show high concentration value on gneiss and very low on quartzite. This implies that during the design of the template both contrasting signatures are present. Thus the algorithm matches the information giving the desired boundary. While the result of template matches using potassium give poor result for both boundaries (Figure 5.9c & 5.10c). Template match results obtained using this image is result of local variability and not related to major variations reflected in different rock units. This could be related to high solubility and mobility of potassium under weathering conditions. Potassium is leached out from the felsic rocks where it was expected to be high and shows no significant variation for the design of the template considering these specific boundaries. In addition from the results obtained using stack of thorium and uranium with potassium show poor response as compared to using single thorium, uranium (Figure 5.9f & 5.10f).

5.4.2. Applied to analytical signal of total magnetic intensity

Results of template match using analytical signal show similar response by giving red line for the presence of contrasting signatures (Figure 5.11). In Figure 5.11a positive match pixels form closed polygons, however none of this pixels meet the boundary considered. Figure 5.11b shows match pixels forming red lines. It is observed that double boundary line that follows the trend of the boundary between sandstone and granite; which are not observed on the other data. This could be due to the magnetic anomaly found in subsurface. Other match results also shown cutting through the granite unit and it could be related to geological structures which are reflected on the magnetic data.

5.4.3. Applied to ASTER ratio image

The output of template match obtained using ASTER image does not indicate presence of significant contrasting signatures for both boundaries (Figure 5.12). Cluster of small red lines scattered in the entire image which have no any coherence to form boundary at all.

From the results obtained it is clear that the RTM algorithm fall to detect boundary using ASTER image. The possibility of mapping lithological contacts using ASTER in the area is hindered due to the lack of information on the image. Vegetation cover of the area affected the remote sensing detection of lithological contacts in the area.

Lithological boundary detection using multi-sensor remote sensing imagery for geological interpretation

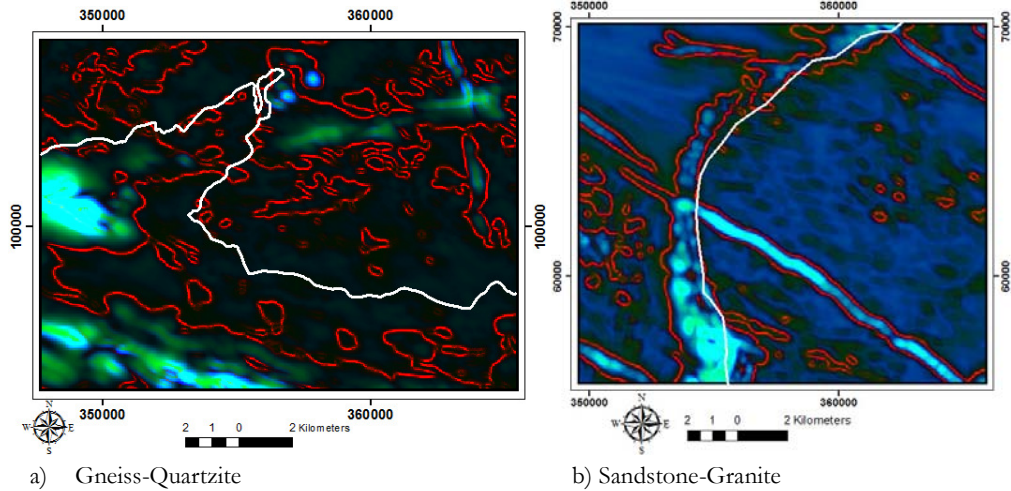


Figure 5-11: Template matching result from Analytical signal. The white line indicates the position of boundary on geological map

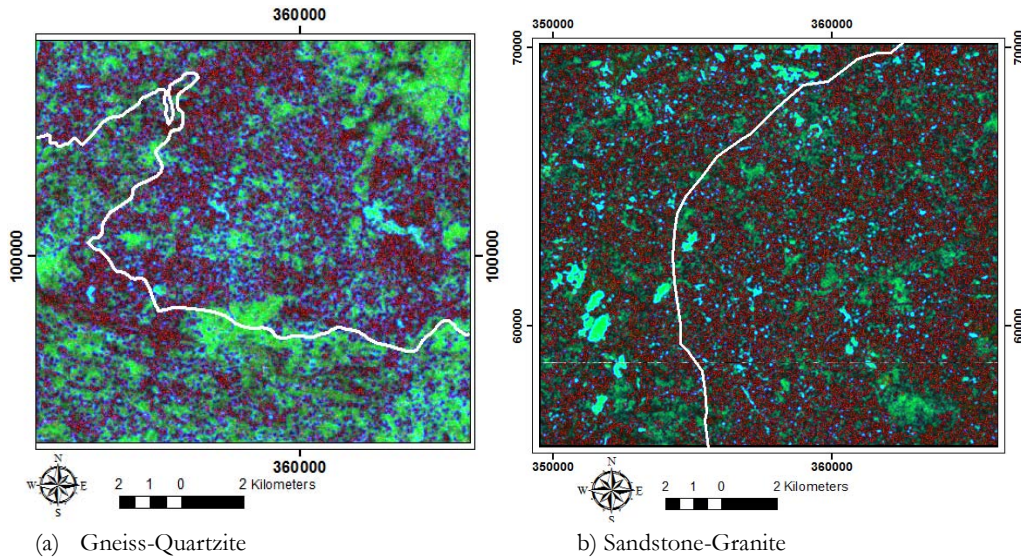


Figure 5-12: Template matching result from ASTER ratio images. The white line indicates the position of boundary on geological map

5.5. Comparison of edge detection results

Matching results obtained from edge detection and template matching methods are compared based on the position of the boundaries on geological map. The effects of threshold on ratio images from template matching results are presented in section 5.5.2.

5.5.1. Edge detection versus RTM template matching results

In this section results from edge detection and RTM template matching using thorium (Th), uranium (U), thorium-uranium (Th+U), potassium-thorium (K+Th), potassium-thorium-uranium (K+Th+U) and analytical signal (AS) are assessed.

In order to compare the matching results, 200m buffer area was produced on both boundaries (b1 and b2) (Figure 5.13a & b) on geological map. Thus the percentage of those pixels at 1.5% cut off from different data set and methods calculated in the buffer zone are shown in Figure 5.14.

Lithological boundary detection using multi-sensor remote sensing imagery for geological interpretation

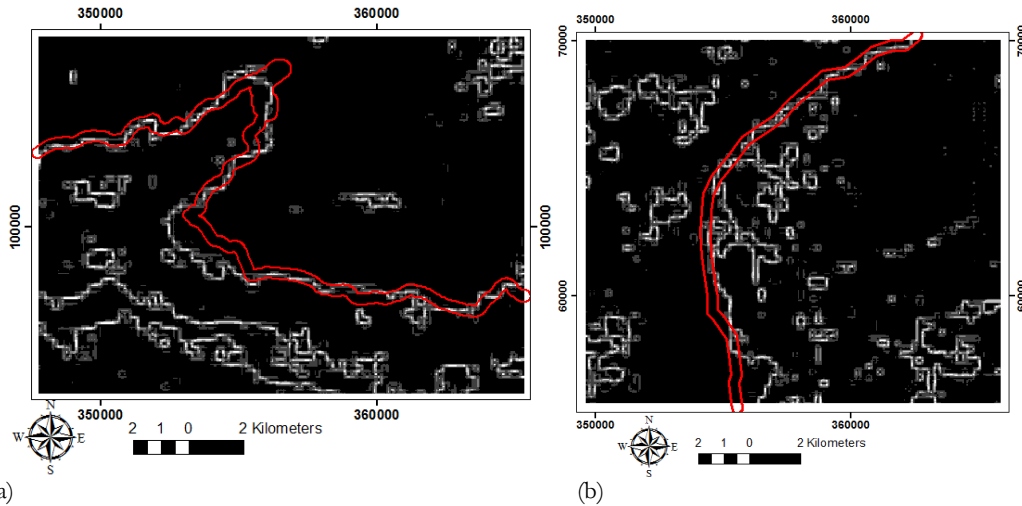
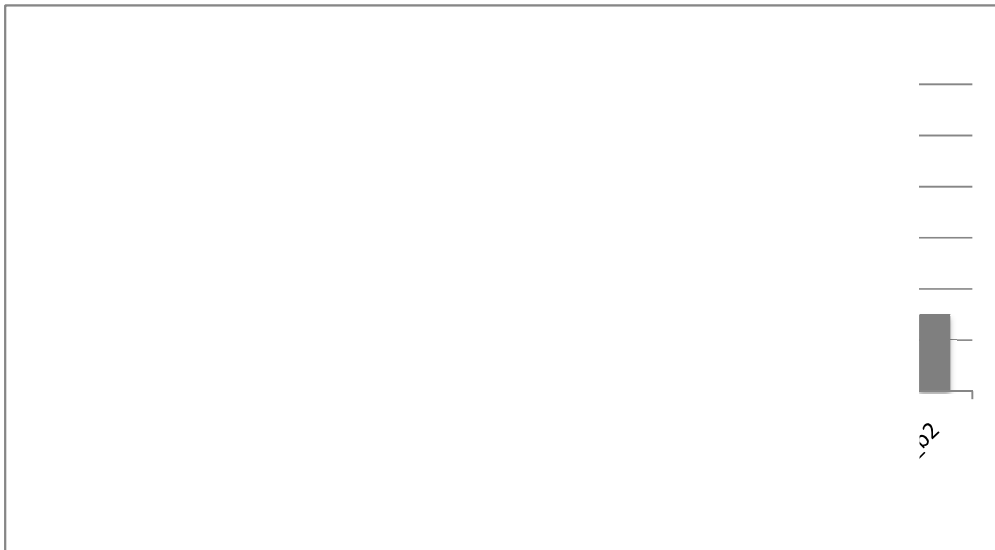


Figure 5-13: maps showing buffers of 200m around boundary one (a) and two (b) on geological map overlain on ratio maps

From the Figure (5.14 a & b), the matching results obtained by template matching show good match results as compared to edge detection results from the single and multiple layer images used. Figure (5.14a) shows template matching results obtained using single and multiple images for both boundaries b1 and b2. In this case better matching results are obtained for b1 as compared to b2 for the particular images used. For example, if we consider thorium and uranium images; good matching results are obtained for b1 than b2. The result obtained from multiple layers used indicate that only the result obtained from thorium-uranium image gives good result even if it doesn't improve the result obtained by using thorium alone. The matching results obtained from potassium-thorium and thorium-uranium-potassium give poor results. Any layer combined with potassium does not give better result being good by itself. The result from analytical signal shows only few fit pixels for the boundary. This could be because the analytical signal reflects in this case sub surface features than surface.



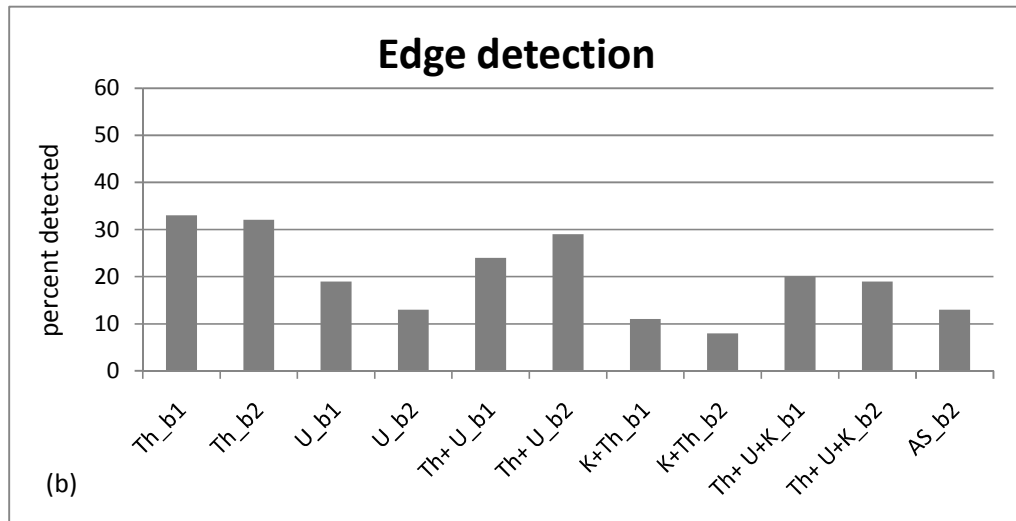


Figure 5-14: Comparison of template matching (a) and edge detection (b) results using 200m buffer area on both b1 and b2 on geological map.

The matching results obtained from edge detection method (Figure 5.14b) show that used thorium image give good matching result for both boundaries compared to other images used as single and /or multiple. From multiple images used thorium-uranium give better results than when combination with potassium was used as also observed on template matching results.

5.5.2. Influence of threshold

It was observed from the results obtained from edge detection algorithms that lithological boundaries are well detected on remote sensing images like thorium and uranium. These images give better discrimination of lithological unit considered in this stud. In this case the results obtained from RTM template matching method give a clear boundary line. Thus template matching output of some ratio image of rotation variance and mean spectral variance are taken and a buffer zone of 80m (Figure 5.15) was produced to determine edge and none edge pixels. The thresholds are defined such that above the threshold value pixels were considered as edge pixels while below the threshold are none edge. Bright pixels are regarded as edge pixels in the edge map and dark ones as none edge. The threshold was determined for ratio images from thorium, uranium, thorium-uranium and potassium-thorium-uranium.

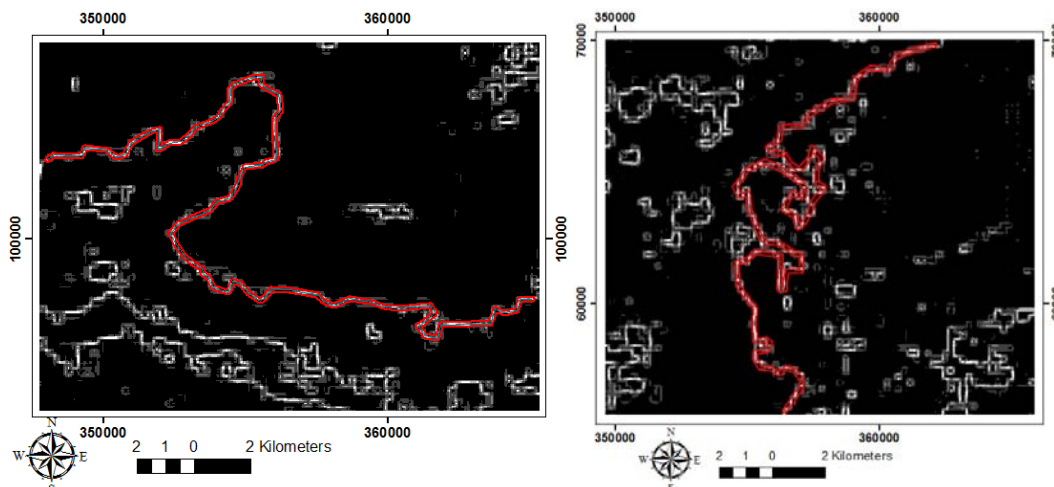


Figure 5-15: 80m buffer area around the boundaries detected

Lithological boundary detection using multi-sensor remote sensing imagery for geological interpretation

The threshold values for each ratio image were objectively chosen in order to evaluate the ratio image on both boundaries. The first threshold was chosen at the natural break for the back ground (none edge) and edge pixels, for each images and then increasing the threshold value by fixed value for all edge pixels. The natural break values could be different depending on the strength of pixels in every ratio image.

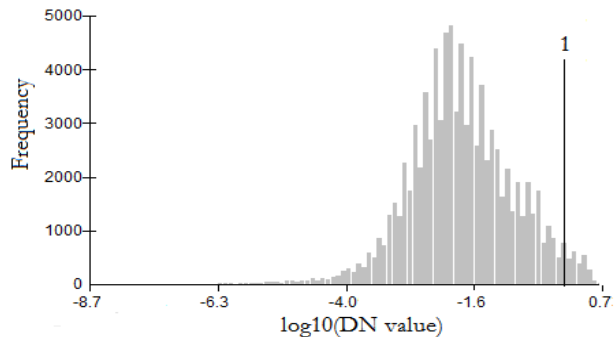
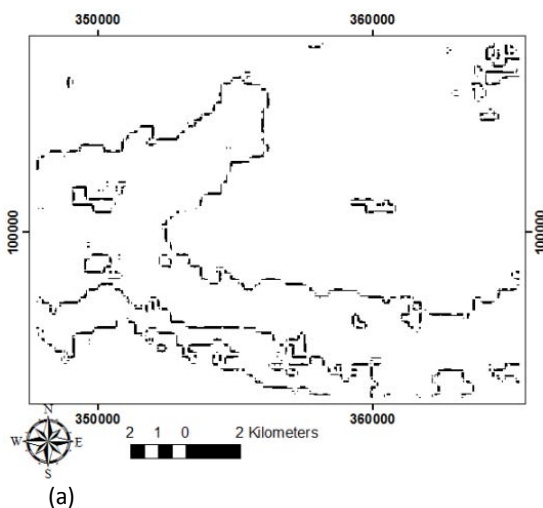
Considering boundary one first, it was observed that; initially the total number of pixels present in the buffer zone on thorium ratio image was 7.6 % of the total pixels detected in the image. Number of pixels retained above threshold 1 are 2.7% which regarded as edge pixels and pixels form a clear continuous line (Figure 5.16a). Figure 5.16b shows the distribution for edge pixels and threshold value. As shown from the corresponding graph (Figure. 5.16c), ratio of edge pixels retained in the buffer zone to those outside at each threshold values is constant. This indicates that most of the pixels get closer strength above the initial threshold hence increasing the threshold value not only remove none edge pixels also edge pixels are removed.

The number of pixels inside the buffer zone was decreased to 5% on uranium ratio image (Figure 5.17). Out of the 5% pixels inside the buffer zone only 1.8% was retained at the first threshold. Figure (5.17 a, b &c) shows uranium ratio image at the initial threshold, histogram of pixels and graph with percent of pixels retained at each threshold values respectively. The ratio image shows the trend of boundary one clearly even if the number of pixels decreased as compared to thorium. Scattered edge pixels are observed outside the buffer zone.

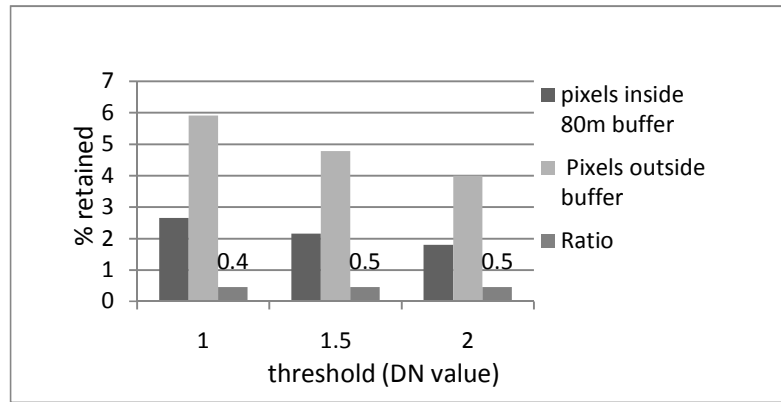
Result from threshold of thorium-uranium edge image (Figure 5.18) give almost similar response as thorium, it gives clear line for boundary one and also pixels outside the buffer zone show more coherence forming clear polygons. The initial number of pixels inside the buffer zone 7% which decreased to 2.5% at the initial threshold. The ratio of pixels inside the buffer to those outside is still constant showing the strength of the edge pixels.

Figure 5.19 shows the effect of threshold on thorium-uranium-potassium ratio image. The total number of pixels inside the buffer zone 5.6% is decreased to 1.5% at threshold initial. In this case, the edge pixels in side buffer zone retained at this threshold value lack connectivity. In addition more scattered pixels are observed in the entire image which couldn't form closed polygons. Removing more pixels increasing the threshold value results in removing the pixels belong to the boundary.

High ratio for the edge pixels inside to outside the buffer area are observed on thorium-uranium as shown in (Figure 5.18c). The ratios also increases as threshold increase indicating that more none edge pixels from outside buffer area are removed than from inside. Ratios obtained from other images remain constant and also the value is less.

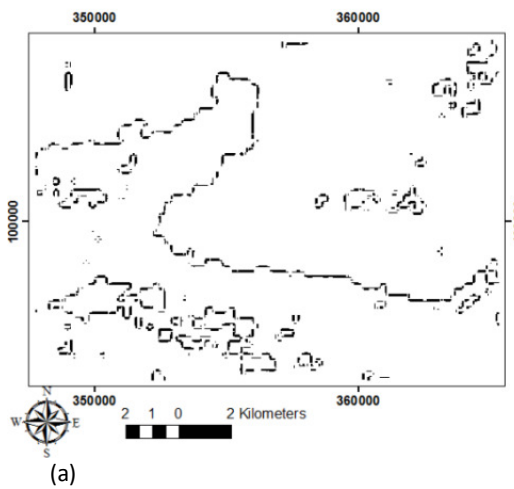


Lithological boundary detection using multi-sensor remote sensing imagery for geological interpretation

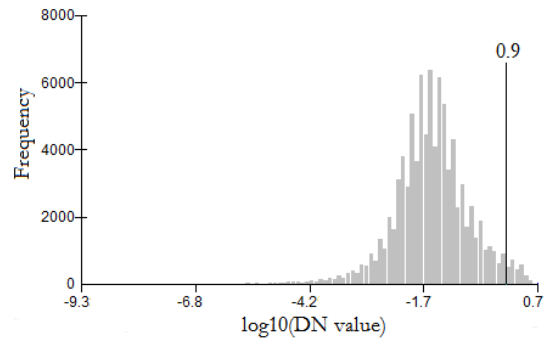


(c)

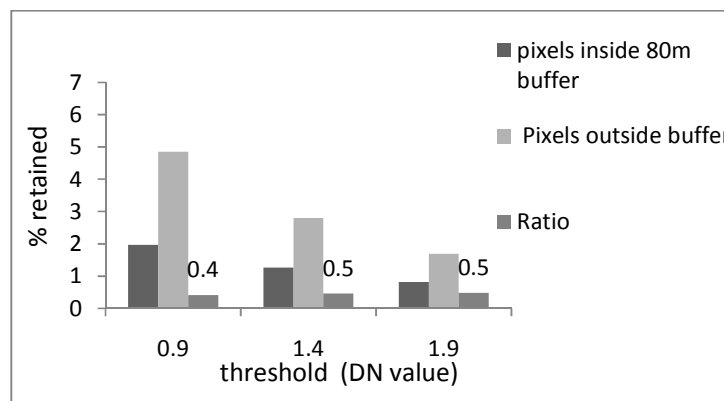
Figure 5-16: Rratio image of thromium showing b1 at initial threshold (a), graph showing distribution of detected pixels on the entire area. the DN value are converted to logarithmic scale in order to empasize the significance of values at the tail of the histogram and considered as edge pixels (b) and the third graph shows the percentage of pixels detected inside and outside the buffer zone and also their ratio as the threshold increases (c)



(a)



(b)



(c)

Figure 5-17: Ratio image of uranium showing boundary one at initial threshold (a), graph showing distribution of detected pixels on the entire area. the DN value are converted to logarithmic scale in order to empasize the significance of values at the tail of the histogram and considered as edge pixels (b) and the third graph shows the percentage of pixels detected inside and outside the buffer zone and also their ratio as the threshold increases (c)

Lithological boundary detection using multi-sensor remote sensing imagery for geological interpretation

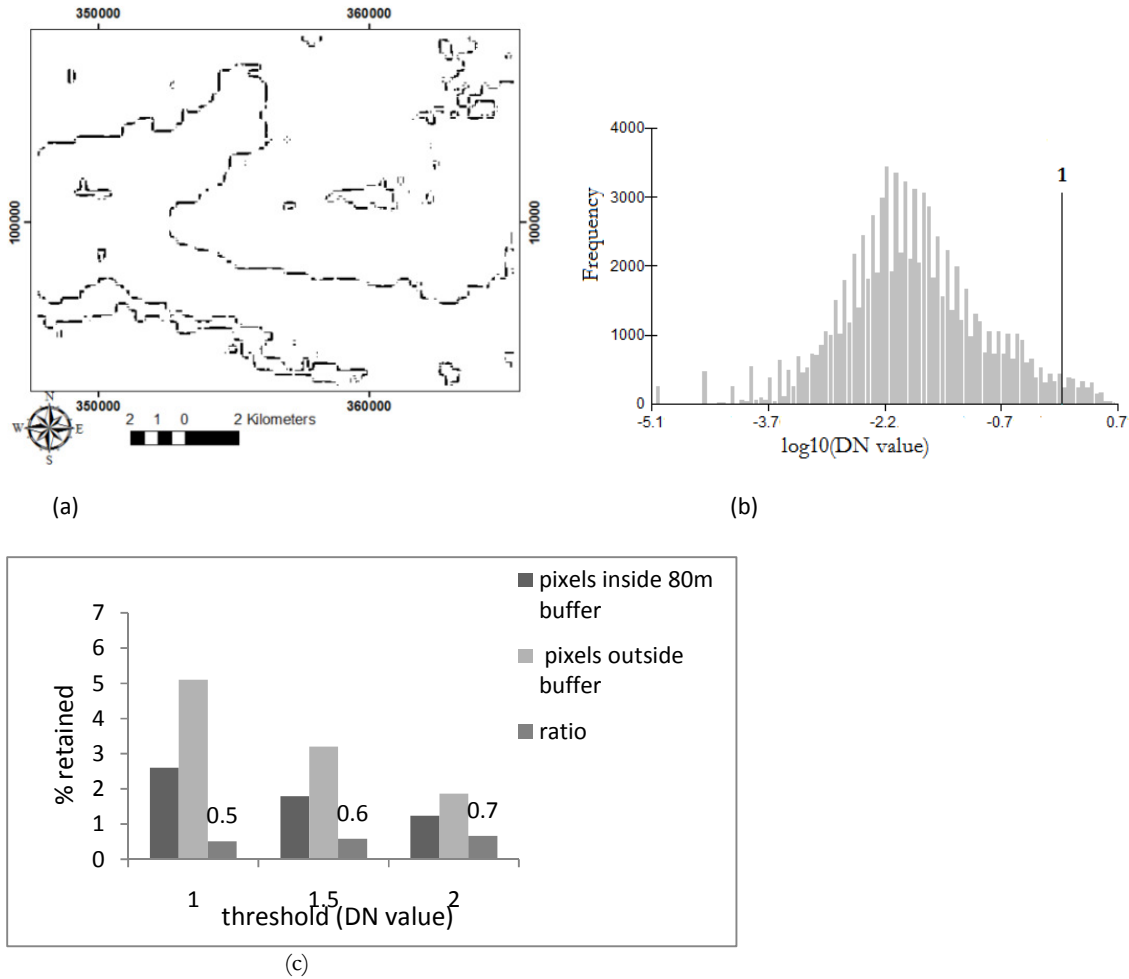
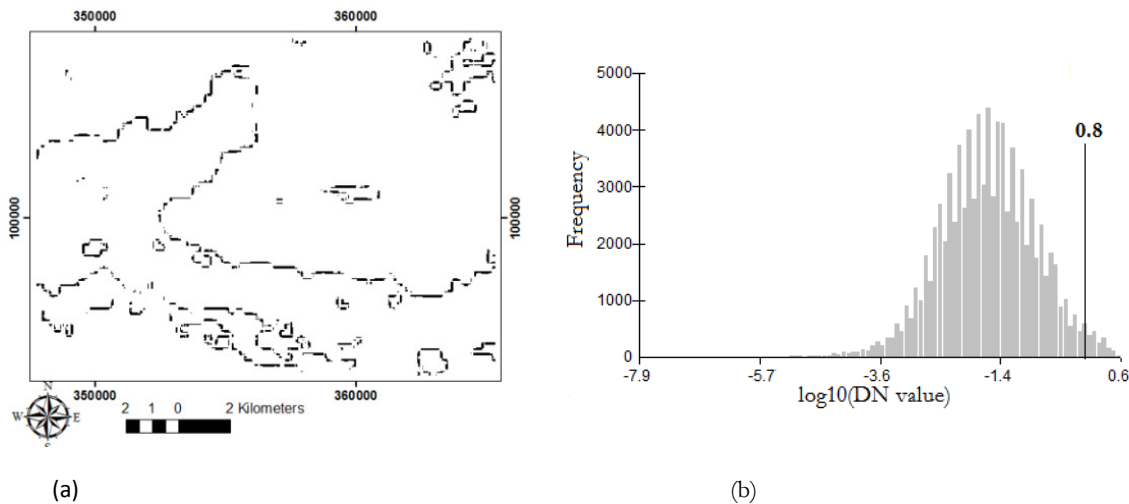
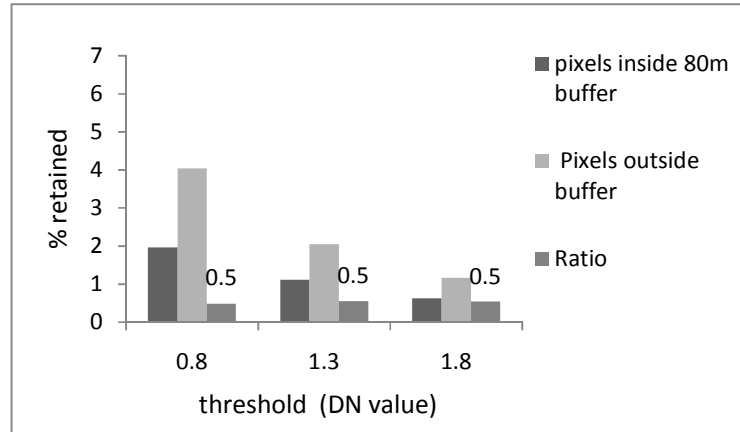


Figure 5-18: Ratio image of throm-uranium showing boundary one at initial threshold (a), graph showing distribution of detected pixels on the entire area. the DN value are converted to logarithmic scale in order to emphasize the significance of values at the tail of the histogram and considered as edge pixels (b) and the third graph shows the percentage of pixels detected inside and outside the buffer zone and also their ratio as the threshold increases (c)





(c)

Figure 5-19 : Ratio image of throrim-uranium-potassium showing boundary one at initial threshold (a), graph showing distribution of detected pixels on the entire area. the DN value are converted to logarithmic scale in order to empasize the significance of values at the tail of the histogram and considered as edge pixels (b) and the third graph shows the percentage of pixels detected inside and outside the buffer zone and also their ratio as the threshold increases (c)

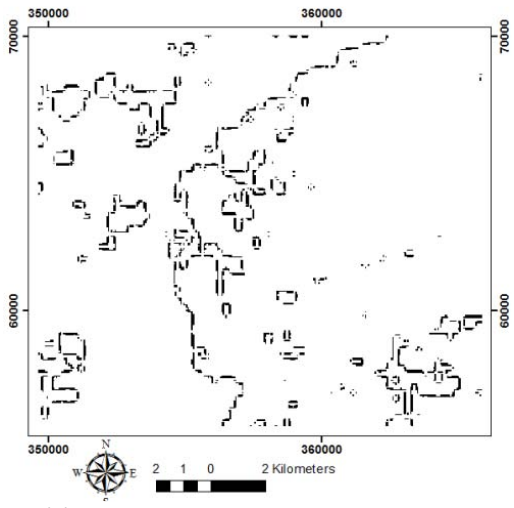
The effect of threshold on b2, the present of pixels retained at each initial threshold value for all images is smaller as compared to boundary one. At the initial threshold, 1.2% out of 3.5% pixels retained in the buffer on thorium at this threshold the pixels forming boundary are clearly observed (Figure 5.20a). As the threshold increases both pixels inside and outside buffer are removed at the same rate indicating closeness of pixels strength (Figure 5.20c). It is also observed that the present of edge pixels outside the buffer are greater and most of which form closed polygons and few are scattered.

In case of uranium (Figure 5.21), 1.3% pixels are retained at the initial threshold out of 3.6% detected and belong to boundary two. The retained pixels are observed to form the boundary at the initial threshold. Ratio of pixels inside to outside the buffer is again remaining constant at each threshold values showing the strength of pixels.

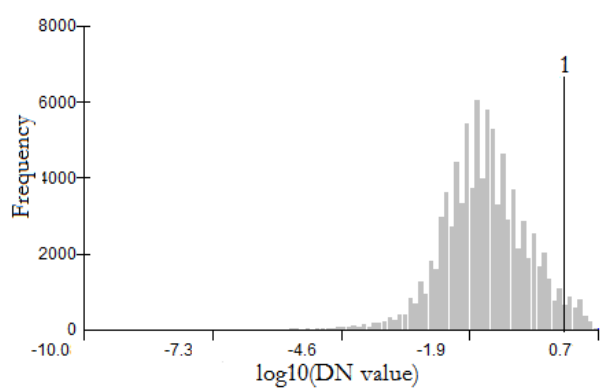
The effect of threshold on thorium-uranium (Figure 5.22) gives similar response as thorium. Pixels retained in buffer at initial threshold forming the boundary and increasing the threshold have effect on both inside and outside buffer. Most of pixels outside the buffer are observed to form closed polygons. Considering the effect of threshold on thorium-uranium-potassium (Figure 5.23), at the initial threshold only 0.8% pixels are retained which could not form a continuous connectivity. Pixels outside the buffer are also reduced and the ratio remains constant as increasing the threshold.

The ratios of pixels inside with pixels outside the buffer area get high value for b2 on uranium ratio image which is 0.4 (Figure 5.21c). On the other hand the ratios are decreased by half as can be seen in Figures (5.20c, 5.22c & 5.23c). This indicates that more edge pixels are detected in for boundary two using uranium and the less edge pixels are found outside the buffer.

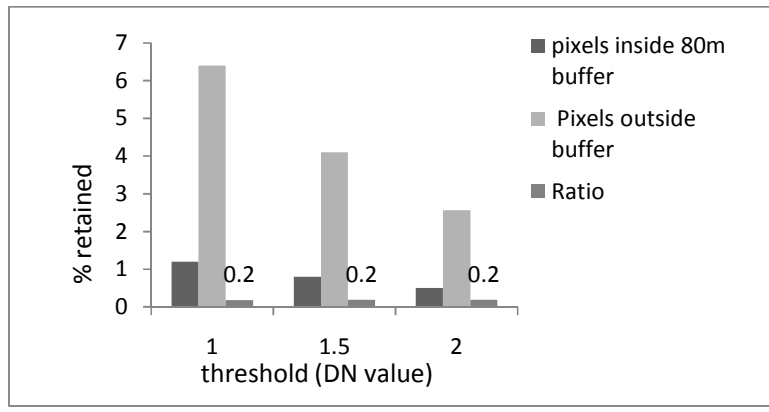
Lithological boundary detection using multi-sensor remote sensing imagery for geological interpretation



(a)

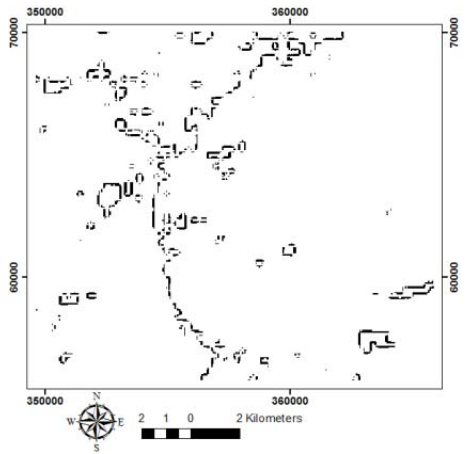


(b)

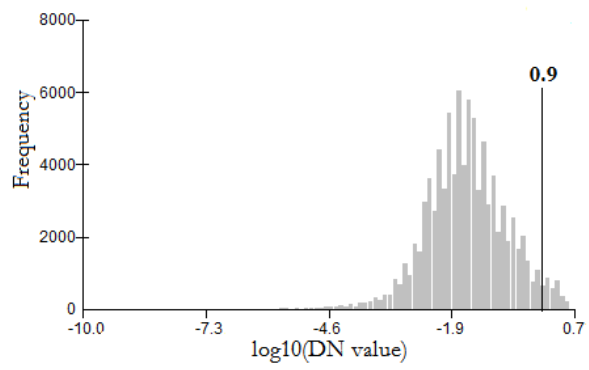


(c)

Figure 5-20: Ratio image of thorium showing b2 at initial threshold (a), graph showing distribution of detected pixels on the entire area. the DN value are converted to logarithmic scale in order to empasize the significance of values at the tail of the histogram and considered as edge pixels (b) and the third graph shows the percentage of pixels detected inside and outside the buffer zone and also their ratio as the threshold increases (c)

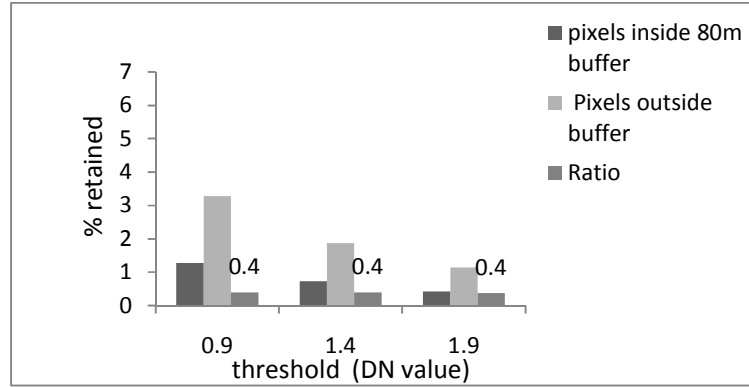


(a)



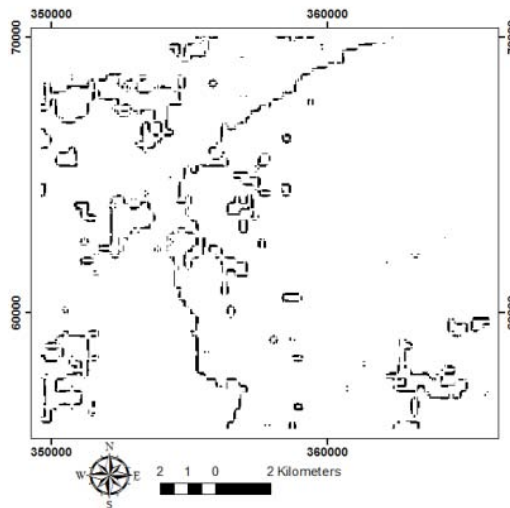
(b)

Lithological boundary detection using multi-sensor remote sensing imagery for geological interpretation

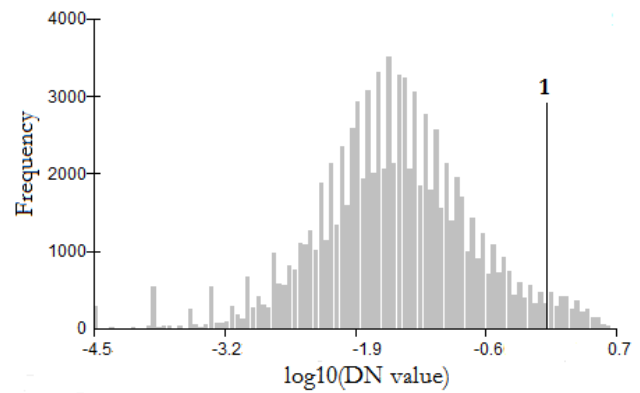


(c)

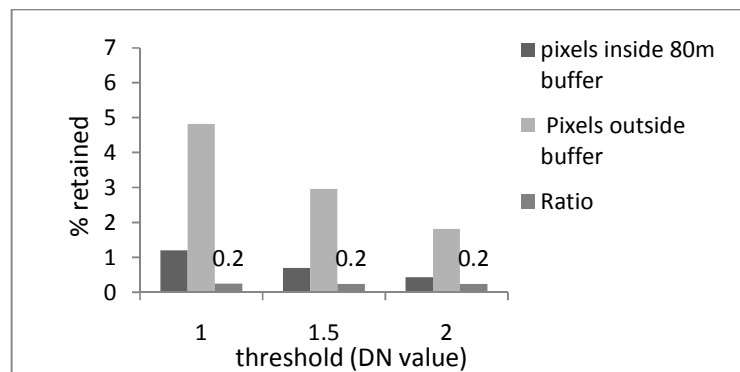
Figure 5-21: Ratio image of uranium showing b2 at initial threshold (a), graph showing distribution of detected pixels on the entire area. the DN value are converted to logarithmic scale in order to emphasize the significance of values at the tail of the histogram and considered as edge pixels (b) and the third graph shows the percentage of pixels detected inside and outside the buffer zone and also their ratio as the threshold increases (c)



(a)



(b)



(c)

Figure 5-22: Ratio image of thorium-uranium showing b2 at initial threshold (a), graph showing distribution of detected pixels on the entire area. the DN value are converted to logarithmic scale in order to emphasize the significance of values at the tail of the histogram and considered as edge pixels (b) and the third graph shows the percentage of pixels detected inside and outside the buffer zone and also their ratio as the threshold increases (c)

Lithological boundary detection using multi-sensor remote sensing imagery for geological interpretation

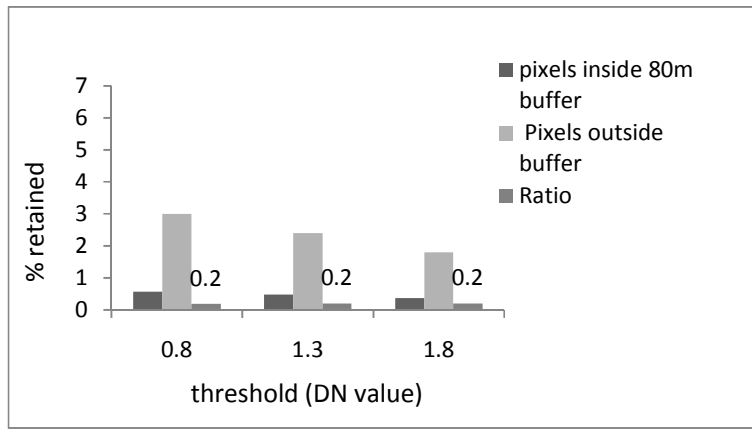
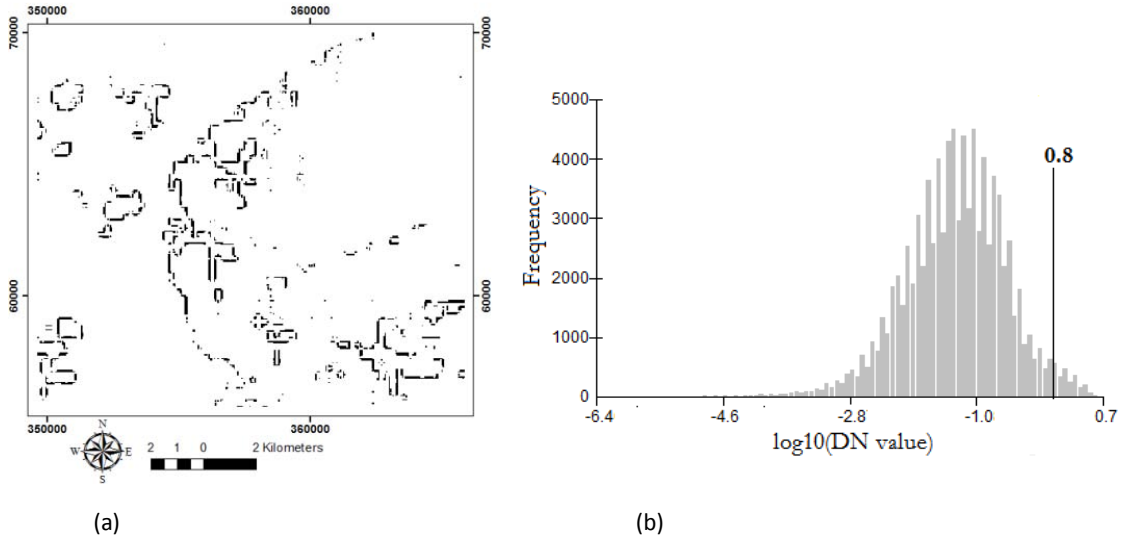


Figure 5-23: Ratio image of thorium-uranium-potassium showing b2 at initial threshold (a), graph showing distribution of detected pixels on the entire area. The DN value are converted to logarithmic scale in order to emphasize the significance of values at the tail of the histogram and considered as edge pixels (b) and the third graph shows the percentage of pixels detected inside and outside the buffer zone and also their ratio as the threshold increases (c)

6. CONCLUSION AND RECOMMENDATION

The study presents the use of field data, edge detection and rotation variant template matching algorithms for lithological boundary mapping.

- Mapping lithological contacts in the field was greatly influenced by the presence of in situ weathering and vegetation cover of the area. The locations of boundary estimated at some field observation points were not feet the boundary on geological map and also those detected on remote sensing imageries. In such areas covered by vegetation and weathering field observations are not helpful for lithological contact mapping.
- Edge detection algorithms were able to extract lithological boundaries between spectrally contrasting signatures. In particular RTM template matching algorithm was able to extract boundaries indicating it as clear contact line. In this case thorium and uranium give good result for mapping lithological contacts considered in this study.
- From the results obtained using multiple data layers, thorium-uranium stack image give good result even if it doesn't improve the result obtained using single thorium image. Other multiple layers used, for example thorium-potassium stack image give even the worst result than obtained using single thorium image. This could be due to the fact that potassium was not good for mapping lithological boundaries in this study area. Thus it can be concluded that adding several data layers do not increase the accuracy of boundary detection being the individual layers give poor result in this case.
- The algorithms were able to detect lithological boundaries under vegetation cover and weathering using thorium and uranium.
- Not all boundaries detected represent lithological boundaries. For example the result obtained from analytical signal of total magnetic intensity reflects some subsurface features unrelated to lithological boundaries.

Even if locating the exact position of lithological boundaries was difficult, field observation on both sides of the boundary was useful in selecting end members for the design of the template. The exact locations of lithological contacts are obscured and only estimation could be made in the field. whereas in such cases gamma ray spectrometry provide information on the variations of radioelement concentrations in rocks and soils and can be used for the discrimination of different lithological units. Since major variations in radioelement concentrations in rocks and soils indicate broad lithological differences that can be mapped.

Edge detection using gradient in all directions and Euclidean distance measure was able to detect boundary zones indicating high and low variability areas. The rotation variant template matching method extracted lithological contacts between spectrally contrasting signatures by indicating the boundary with a clear line. From the visual interpretation of the results, both methods give good results using thorium, uranium and thorium-uranium, while, the result was not good in identifying both boundaries using potassium, thorium-potassium and thorium-uranium-potassium images. Results obtained using analytical signal shows contacts of subsurface structures unrelated to lithological boundary in both case. The RTM algorithm fall to detect boundaries using ASTER image. The vegetation cover and weathering obscure the remote sensing detection of lithological units in this area.

Results obtained from both matching results were evaluated using a 200m buffer area for both boundaries on geological map. From the comparison matching result obtained from template matching give better matching result compared to edge detection results. The ratio image of thorium, uranium and thorium-uranium are giving better matching result than any combination with potassium. This is because the variation of potassium in the pair of rock units for example sandstone and granite do not show significant

Lithological boundary detection using multi-sensor remote sensing imagery for geological interpretation

contrast and hence give poor result when used as single and combined with other images. Also the result obtained from the matching of analytical signal give the least, because most of the edges detected do not correspond with lithological contacts considered; rather reflects geological features found in subsurface.

The RTM template matching algorithm show good performance by providing a consistent result for mapping contacts between two contrasting signatures. Hence could be remarkable to use the method for similar purpose.

LIST OF REFERENCES

- A.L. Jaques, P.W., A. Whitaker & D. Wyborn, 1997, High resolution geophysics in modern geological mapping: AGSO Journal of Australian Geology & Geophysics, p. 159-173.
- B.L. Dickson, and Scott, K.M., 1997, Interpretation of aerial gamma-ray surveys-adding the geochemical factors: AGSO Journal of Australian Geology & Geophysics, p. 187- 200.
- Bakker, W.H., and Schmidt, K.S., 2002, Hyperspectral edge filtering for measuring homogeneity of surface cover types: ISPRS Journal of Photogrammetry and Remote Sensing, v. 56, p. 246-256.
- Canny, J., 1986, A Computational approach to edge detection: IEEE Transactions Pattern Analysis and Machine Intelligence, v. Vol. 8, p. pp.679- 697.
- Cheng, H.D., Jiang, X.H., Sun, Y., and Wang, J., 2001, Color image segmentation: advances and prospects: Pattern Recognition, v. 34, p. 2259-2281.
- Cumani, A., 1991, Edge detection in multispectral images: CVGIP: Graphical Models and Image Processing, v. 53, p. 40-51.
- Finn, C.A., and Morgan, L.A., 2002, High-resolution aeromagnetic mapping of volcanic terrain, Yellowstone National Park: Journal of Volcanology and Geothermal Research, v. 115, p. 207-231.
- Gad, S., and Kusky, T., 2007, ASTER spectral ratioing for lithological mapping in the Arabian-Nubian shield, the Neoproterozoic Wadi Kid area, Sinai, Egypt: Gondwana Research, v. 11, p. 326-335.
- Hewson, R.D., Cudahy, T.J., Mizuhiko, S., Ueda, K., and Mauger, A.J., 2005, Seamless geological map generation using ASTER in the Broken Hill-Curnamona province of Australia: Remote Sensing of Environment, v. 99, p. 159-172.
- Hou, Z.J., and Wei, G.W., 2002, A new approach to edge detection: Pattern Recognition, v. 35, p. 1559-1570.
- Kalubandara, S.T., 2005, Mapping of mineral transitional zones by an image template matching method: Enschede, ITC.
- Mavrantza, O., and Argialas, D., 2008, An object-oriented image analysis approach for the identification of geologic lineaments in a sedimentary geotectonic environment, *in* Blaschke, T., Lang, S., and Hay, G.J., eds., Object-Based Image Analysis: Lecture Notes in Geoinformation and Cartography, Springer Berlin Heidelberg, p. 383-398.
- Méndez Alves, M.V., 2007, Detection of physical shoreline indicators in a object - based classification approach : study case, Island of Schiermonnikoog, The Netherlands: Enschede, ITC.
- Nyakairu, G.W.A., Kurzweil, H., and Koeberl, C., 2002, Mineralogical, geochemical, and sedimentological characteristics of clay deposits from central Uganda and their applications: Journal of African Earth Sciences, v. 35, p. 123-134.
- Oluwafemi, O., 2010, Lithologic boundary detection in hyperspectral imagery, using spatial - contextual algorithms in Cabo de Gata, SE Spain.: Enschede, University of Twente Faculty of Geo-Information and Earth Observation ITC, Enschede.
- Peli, T., and Malah, D., 1982, A study of edge detection algorithms: Computer Graphics and Image Processing, v. 20, p. 1-21.
- Qureshi, S., 2005, Edge Detection and Segmentation, Embedded Image Processing on the TMS320C6000™ DSP, Springer US, p. 211-280.
- R.J. Johnson, and Williams, C.E.F., 1961, Explanation of the Geology of Sheet 59 (Kiboga), Geological Survey of Uganda.
- Rowan, L.C., and Mars, J.C., 2003, Lithologic mapping in the Mountain Pass, California area using Advanced Spaceborne Thermal Emission and Reflection Radiometer (ASTER) data: Remote Sensing of Environment, v. 84, p. 350-366.
- Schluter, T., 2006, Geological Atlas of Africa with notes on Stratigraphy, Tectonics, Economic Geology, Geohazards and Geocites of Earth Country, Geological Atlas of Africa, Springer Berlin Heidelberg, p. 238 - 241.
- Shufelt, J., 2000, Geometric constraints for object detection and delineation, Kluwer Academic Publishers
- Torre, V., and Poggio, T.A., 1986, On Edge Detection: Pattern Analysis and Machine Intelligence, IEEE Transactions on, v. PAMI-8, p. 147-163.
- Tsai, D.-M., and Yang, C.-H., 2005, A quantile-quantile plot based pattern matching for defect detection: Pattern Recognition Letters, v. 26, p. 1948-1962.

- van der Werff, H., van Ruitenbeek, F., van der Meijde, M., van der Meer, F., de Jong, S., and Kalubandara, S., 2007, Rotation-Variant Template Matching for Supervised Hyperspectral Boundary Detection: *Geoscience and Remote Sensing Letters, IEEE*, v. 4, p. 70-74.
- van der Werff, H.M.A., van der Meer, F.D.p., de Jong, S.M.p., and van der Meijde, M.p., 2006, Knowledge based remote sensing of complex objects : recognition of spectral and spatial patterns resulting from natural hydrocarbon seepages: Utrecht, Enschede, Utrecht University, ITC.
- van Ruitenbeek, F.J.A., van der Werff, H.M.A., Hein, K.A.A., and van der Meer, F.D., 2008, Detection of pre-defined boundaries between hydrothermal alteration zones using rotation-variant template matching: *Computers & Geosciences*, v. 34, p. 1815-1826.
- van Ruitenbeek, F.J.A., van der Werff, H.M.A., and van der Meer, F.D., 2006, Process - based mapping using spectral indicators in an image template matching approach: In: *ISPRS 2006 : ISPRS mid-term symposium 2006 remote sensing : from pixels to processes*, 8-11 May 2006, Enschede, the Netherlands. Enschede : ITC, 2006. 5 p.
- Wilford, J., and Minty, B., 2006, Chapter 16 The Use of Airborne Gamma-ray Imagery for Mapping Soils and Understanding Landscape Processes, *in* P. Lagacherie, A.B.M., and Voltz, M., eds., *Developments in Soil Science*, Volume Volume 31, Elsevier, p. 207-218, 609-610.
- Wilfrod, J.R., Bierwirth, P.N., and Craig, M.A., 1997, Application of airborne gamma ray spectrometry in soil/regolith mapping and applied geomorphology: *AGSO Journal of Australian Geology & Geophysics*, p. 201- 216.
- Zhu, S.-Y., Plataniotis, K.N., and Venetsanopoulos, A.N., 1999, Comprehensive analysis of edge detection in color image processing: *Optical Engineering*, v. 38, p. 612-625.
- Ziou, D., and Tabbone, S., 1998, Edge Detection Techniques - An Overview: *International Journal of Pattern Recognition and Image Analysis*, v. 8, p. 537- 559.

APPENDICES

Appendix1. Field observation points and description of exposures
Observations
& samples

N0.	Latitude	Longitude	Elevation	Observations & samples	Description
1	335621	72618	1266	UG01_UG-01-10	granite
2	338088	71202	1265	UG02	contact (sandstone), highly weathered,
3	341524	70630	1264	UG03	coarse grained sandstone (quartzitic sandstone)
4	354725	61340	1296	UG04_UG-03-10	granite weathered ,
5	354037	61249	1294	UG05_UG-02-10	sandstone, massive, grey color, sample UG-02-10, contact zone with granite
6	366484	61281	1223	UG06	boulders of granite
7	370557	74187	1225	UG07	boulders of granite
8	369485	79022	1152	UG08	contact to the fine sandstone, sudden change in slope, type of vegetation cover
9	363327	97110	1209	UG09	the contact b/n this rock unit and the gneiss gradational
10	371140	97373	1251	UG10	quartzite ridge
11	374552	93955	1243	UG11	quartzite ridge
12	372186	91598	1205	UG12_UG-05-10	sandstone, low laying than the quartzite, sample UG-05-10
13	376081	91094	1159	UG13_UG-06-10	quartz brachia, sample
14	376597	91744	1162	UG14	brecciated quartzite, coarse, pic taken looking west
15	379962	87996	1402	UG15_UG-07-10	bulaga puluto, sand stone
16	385561	83474	1289	UG16	quartzite
17	382340	88302	1334	UG17	quartzite ridge
18	362756	97554	1232	UG18	granitic gneiss highly weathered
19	363468	96746	1233	UG19_UG-04-10	quartzite ,
20	363859	95190	1193	UG20	gently sloping towards the quartzite unit northwards, (sandstone unit)
21	368560	93671	1167	UG21	quartzite
22	363970	93109	1188	UG22	thick soil cover
23	357075	66365	1139	UG23	highly weathered granite
24	372220	73108	1201	UG24	highly weathered granite
25	376517	68373	1269	UG25	granite

26	356623	63261	1222	UG26	granite, highly weathered
27	379472	65125	1245	UG27	sandstone, highly weathered
28	377335	67909	1236	UG28	highly weathered granite boulders and changing to the soil
29	348012	92076	1129	UG29_UG-08-10	quartzitic sandstone,
30	359587	97524	1130	UG38	quartzite ridge
31	347592	98466	1167	UG30_UG-09-10	quartzite, , ridge forming exposure
32	351573	100179	1167	UG31	quartzite ridge
33	352703	100573	1210	UG32	quartzite outcrop, forming ridge
34	354577	99899	1263	UG33	granitic gneiss,
35	353622	100253	1262	UG34	contact b/n quartzite and granite gneiss, boulders of gneiss and quartzite rocks
36	355848	105998	1230	UG35	quartz and some boulders of gneiss exposed,...contact zone
37	350970	104255	1210	UG36	granite gneiss, about hundred meters away from quartzite ridge to the west
38	343648	102305	1148	UG37	quartzite
39	363985	99552	1212	UG39	granitic gneiss
40	384652	84870	1265	UG40	quartzite, contact b/n sandstone
41	371709	60968	1248	UG41	highly weathered, thick soil cover
42	362175	93291	1220	UG42	weathered soil, fine sandstone
43	345327	103874	1237	UG43	weathered gneiss, boulders
44	355814	99162	1249	UG44	weathered gneiss, boulders

